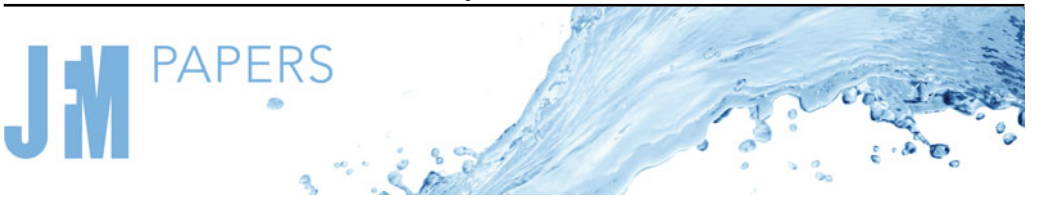
J. Fluid Mech. (2025), *vol.* 1015, A44, doi:10.1017/jfm.2025.10377



Initial perturbation dependence on Richtmyer–Meshkov instability with reshock

Yumeng Zhang[1], **Yong Zhao**[1], **Zhangbo Zhou**[1], **Juchun Ding**[1,2] and **Xisheng Luo**[1]

[1]State Key Laboratory of High Temperature Gas Dynamics, School of Engineering Science, University of Science and Technology of China, Hefei 230026, PR China

[2]Laoshan Laboratory, Qingdao 266237, PR China

Corresponding authors: Xisheng Luo, xluo@ustc.edu.cn; Juchun Ding, djc@ustc.edu.cn

(Received 4 January 2025; revised 16 May 2025; accepted 16 June 2025)

The Richtmyer–Meshkov instability at gas interfaces with controllable initial perturbation spectra under reshock conditions is investigated both experimentally and theoretically. A soap-film method is adopted to generate well-defined single-, dual- and triple-mode air/SF_6 interfaces. By inserting an acrylic block into the test section, a reflected shock with controllable reshock timing is created. The results reveal a complex relationship between the post-reshock perturbation growth rate and the pre-reshock interface morphology. For single-mode interfaces, the post-reshock growth rate exhibits a strong dependence on pre-reshock conditions. In contrast, for multi-mode interfaces, this dependence weakens significantly due to mode-coupling effects. It is found that, following reshock, each fundamental mode develops independently and later is significantly influenced by mode-coupling effects. Based on this finding, we propose an empirical model that matches the initial linear growth rate and the asymptotic growth rate, accurately predicting the evolution of fundamental modes from early to late stages across all three configurations. Furthermore, a theoretical formula is derived, linking the empirical coefficient in the model of Charakhch'An (2020 *J. Appl. Mech. Tech. Phys.* vol. 41, no. 1, pp. 23–31) to the initial perturbation. This provides a unified framework to explain the varying dependence of post-reshock growth rates on pre-reshock morphology observed in previous experiments.

Key words: shock waves, shear-flow instability

1. Introduction

When a shock wave impinges upon an interface separating two fluids of different property, initial perturbations at the interface first grow linearly, then nonlinearly over time. In

© The Author(s), 2025. Published by Cambridge University Press.

https://doi.org/10.1017/jfm.2025.10377 Published online by Cambridge University Press

the nonlinear regime, the interface undergoes significant distortion, characterised by the formation of spikes (heavy fluid penetrating into light fluid) and bubbles (light fluid rising into heavy fluid), which could potentially lead to a transition to turbulent mixing. This type of hydrodynamic instability is usually referred to as the Richtmyer–Meshkov instability (RMI) (Richtmyer 1960; Meshkov 1969). A similar yet distinct instability is the Rayleigh–Taylor instability (RTI), which occurs as the interface is subjected to continuous acceleration. The RMI exists widely in scientific and industrial fields with scales spanning from millimetre (e.g. inertial confinement fusion, ICF) (Murakami & Nishi 2017; Li, Samtaney & Wheatley 2018) to light year (e.g. supernova explosions) (Kuranz *et al.* 2018). For example, in ICF, instability growth at both the exterior ablator–shell interface and the interior shell–fuel interface (Li *et al.* 2022*b*; Samulski *et al.* 2022) dramatically enhances the mixing between the inner fuel and the outer ablator, leading to a reduction in energy yield or even ignition failure (Lindl *et al.* 2014). However, in scramjets, the mixing of fuel and air, enhanced by RMI, is beneficial for improving combustion efficiency (Urzay 2018).

As a fundamental problem, RMI at a single-mode interface under single shock impact has attracted much attention, and comprehensive reviews have been published on this topic (Zabusky 1999; Brouillette 2002; Ranjan, Oakley & Bonazza 2011; Zhou 2017*a*,*b*). In previous studies, the growth of instability across the linear, nonlinear and turbulent mixing stages has been extensively investigated through experiments (Jacobs *et al.* 1995; Sadot *et al.* 1998; Jacobs & Krivets 2005; Aure & Jacobs 2008; Balakumar *et al.* 2008*b*; Morgan *et al.* 2012; Mansoor *et al.* 2020), simulations (Cloutman & Wehner 1992; Youngs 1994; Latini, Schilling & Don 2007; Youngs & Williams 2008) and theoretical analyses (Zhang & Sohn 1997; Mikaelian 2005; Dimonte & Ramaprabhu 2010; Zhang, Deng & Guo 2018). By modelling the shock impact as an impulsive acceleration (i.e. a Dirac delta function), Richtmyer (1960) developed an impulsive model that provides a simplified yet useful prediction of early-time perturbation growth for single-mode RMI. As nonlinear effects become significant, new harmonics are generated, which feed back into the fundamental mode and gradually reduce its growth rate. To describe nonlinear growth, various theoretical models have been proposed, including perturbation expansion models (Zhang & Sohn 1997; Vandenboomgaerde *et al.* 2002, 2003; Zhang *et al.* 2018), potential flow models (Alon *et al.* 1995; Sohn 2003; Zhang & Guo 2016), vortex models (Samtaney & Zabusky 1994; Jacobs & Sheeley 1996; Samtaney, Ray & Zabusky 1998; Sohn 2011) and empirical models (Dimonte & Ramaprabhu 2010). However, these linear and nonlinear models are limited to single-mode RMI driven by a single shock.

In practical applications, material interfaces typically exhibit multi-mode or random perturbations. Unlike single-mode RMI, the multi-mode case introduces additional complexities, including mode-coupling effects such as harmonic generation and bubble merging, leading to significantly more intricate flow phenomena (Luo *et al.* 2020). These complexities exceed the applicability of existing models developed for single-mode RMI. Furthermore, in real-world scenarios, the incident shock wave, after interacting with a perturbed interface, may reflect from either a geometric centre or a solid wall, subsequently re-impacting the interface. To date, only a preliminary understanding of reshocked RMI mechanisms has been achieved through a limited number of experimental and numerical studies. For small-amplitude single-mode interfaces, shock-tube experiments by Weber *et al.* (2012) and Zhang *et al.* (2023*b*) demonstrated a strong dependence of the post-reshock growth rate on pre-reshock conditions, including interface morphology and growth rate. Similarly, Guo *et al.*'s (2022*b*) experiments with large-amplitude single-mode interfaces confirmed this significant dependence. In contrast, studies on reshocked RMI at random multi-mode interfaces, such as those by Vetter & Sturtevant (1995) and Leinov *et al.* (2009), revealed that the post-reshock growth rate is independent of the pre-reshock

https://doi.org/10.1017/jfm.2025.10377 Published online by Cambridge University Press

interface shape and growth rate. This behaviour is particularly challenging to reconcile with the widely accepted view that RMI evolution is highly sensitive to initial conditions prior to shock impact. Recent experiments have further revealed complex behaviours in reshocked RMI at multi-mode interfaces. Ferguson & Jacobs (2024) investigated the interaction of successive shocks with a multi-mode interface, highlighting the significant influence of shock-to-reshock time on the large-scale Reynolds number. Sewell *et al.* (2021) examined the growth rates of randomly perturbed multi-mode interfaces subjected to a reflected shock, finding different growth exponents for small- and large-amplitude perturbations. By using Faraday waves to create a three-dimensional random interface, Jacobs, Krivets & Tsiklashvili (2013) identified two distinct power-law regimes before reshock, followed by a consistent linear growth after reshock. Balakumar *et al.* (2008*a*) investigated light–heavy–light gas curtains subjected to incident and reflected shocks, observing significant increases in mixing width and mixing level immediately after reshock. Balasubramanian *et al.* (2012) used a movable end wall to control reshock timing, finding that high-wavenumber perturbations accelerate turbulence onset. A subsequent study by Balakumar *et al.* (2012) quantified the post-reshock velocity and density statistics. Also, Mohaghar *et al.* (2017, 2019) explored reshock-induced RMI at single- and multi-mode interfaces, focusing on the effects of initial conditions, Mach number and interface morphology on turbulent transition. More recently, Noble *et al.* (2023) examined the evolution of turbulent kinetic energy and scalar spectra after reshock, demonstrating that scalar spectra adhere to a scaling consistent with the Gibson relation (Gibson 1968). In multi-mode RMI, nonlinear effects are more pronounced, adding further complexity to theoretical analysis. Under reshock conditions, the interplay between nonlinearity and reshock effects creates even more intricate flow regimes. As a result, the underlying mechanisms of multi-mode RMI under reshock remain poorly understood, highlighting the need for further investigation and motivating the present study.

Several empirical models have been developed to predict the perturbation growth rate following reshock. A simple linear superposition model, proposed by Mikaelian (1985), sums the growth rates induced by both the incident and reflected shocks. This model suggests that the post-reshock growth rate is influenced by both the pre-reshock growth rate and the interface shape. Similarly, numerical studies by Charakhch'An (2000) confirmed a strong correlation between the post-reshock growth rate and the pre-reshock growth rate, although the dependence on the pre-reshock interface shape was found to be weak. Based on these findings, Charakhch'An (2000) proposed an empirical model applicable under specific conditions outlined in their study. In contrast, Mikaelian (1989) observed that for reshocked RMI at initially three-dimensional multi-mode interfaces, the post-reshock growth rate can be independent of both the pre-reshock interface shape and growth rate. This underscores the existence of more complex relationships between the post-reshock growth rate and pre-reshock variables under certain conditions. Currently, a unified model capable of explaining these diverse observations is lacking, further motivating the present study.

In this work, we will investigate reshocked RMI through high-fidelity shock-tube experiments using interfaces with precisely controlled perturbation spectra, including single-, dual- and triple-mode configurations. These experiments reveal both the perturbation growth patterns and their dependence on initial conditions. Building on these observations, we develop a theoretical model that incorporates mode-coupling effects to predict post-reshock perturbation growth. Furthermore, by deriving a theoretical formula that links the empirical coefficient in Charakhch'An's (2000) model to the characteristics of the initial perturbations, we provide a unified framework to explain the varying sensitivity of post-reshock growth rates to pre-reshock morphology observed in prior experiments.

https://doi.org/10.1017/jfm.2025.10377 Published online by Cambridge University Press

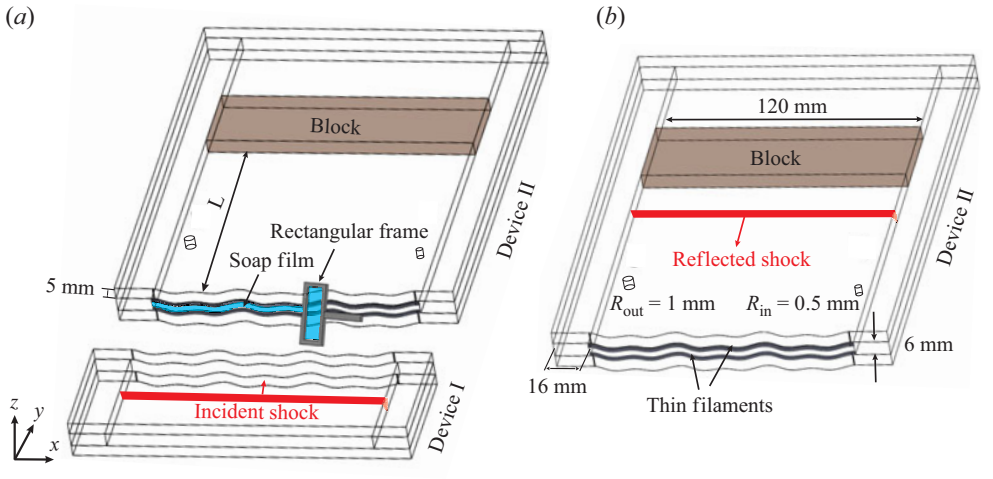


Figure 1. Schematic diagrams showing (*a*) the formation of the initial interface and (*b*) the generation of the reflected shock.

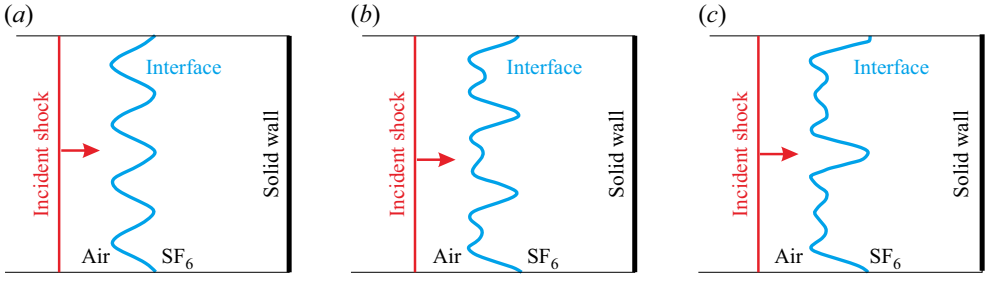


Figure 2. Sketches of the experimental set-up for the reshocked RMI at (*a*) a single-mode interface, (*b*) a dual-mode interface and (*c*) a triple-mode interface.

2. Experimental methods

The experiments are carried out in a horizontal shock tube consisting of three sections: a 1700.0 mm long driver section, a 3900.0 mm long driven section and a 1000.0 mm long test section. The test section has a cross-sectional area of 120.0 × 6.0 mm^2. A soap-film technique developed by Liu *et al.* (2018) is adopted to generate well-characterised discontinuous interfaces that are free of short-wavelength perturbations, three-dimensional effects and diffusion layers. As depicted in figure 1(*a*), two transparent devices, each with an inner height of 6.0 mm and a width of 120.0 mm, are fabricated using 5.0 mm thick acrylic plates. Their adjacent boundaries are engraved carefully to present a desired shape. Two thin filaments, matching the shape of these boundaries, are attached to the upper and lower surfaces of device II, acting as constraints. The protruding height of the filaments into the test section is approximately 0.2 mm, producing a negligible influence on the flow. To facilitate interface formation, the filaments are pre-wetted with a small amount of soap solution composed of 60 % distilled water, 20 % sodium oleate and 20 % glycerine. As a small rectangular frame, dipped with moderate soap solution, is pulled along the upper and lower filaments, a soap film is immediately formed that mirrors the shape of the filaments. To create an air/SF_6 interface, SF_6 gas is injected into device II through an inflow hole, while air is exhausted through an outflow hole. To ensure efficient venting of air and also to minimise the influence of the holes on the flow, the radii of the outflow and inflow holes

https://doi.org/10.1017/jfm.2025.10377 Published online by Cambridge University Press

are set to be 1.0 and 0.5 mm, respectively. In experiment, an oxygen concentration detector is placed at the exit of the outflow hole to continuously monitor the oxygen volume fraction in the exhausted gas. Once the measured volume fraction meets the experimental criterion (below 2 %), devices II and I are inserted successively into the test section to initiate the experiment. Note that the small height of the test section helps to significantly reduce three-dimensionality of the initial interface.

An acrylic block is placed inside device II to facilitate the formation of a reflected shock, as depicted in figure 1(*b*). When an incident shock passes across the gas interface and strikes the inserted block, a reflected shock wave is immediately generated. This reflected shock then propagates upstream, re-accelerating the gas interface in the direction opposite to that of the incident shock. As illustrated in figure 2, in a Cartesian coordinate system, the single-, dual- triple-mode interfaces can be described by

$$y = \sum_{i=1}^{n} a_i^0 \cos(ikx + \phi_i), \quad (n = 1, 2, 3), \tag{2.1}$$

where k is the wavenumber of the first mode ($k = 2\pi/\lambda$, with λ being the wavelength, which varies across different cases), a_i^0 ($i = 1, 2, 3$) denotes the initial amplitude of the ith mode with wavenumber ik. In this work, we set $a_i^0 = 1.0$ mm for all constituent modes. In the present experiment, the time when the reflected shock encounters the interface is precisely controlled by adjusting the distance between the block and the initial interface. The incident shock propagates in air at a Mach number of 1.30 ± 0.02. The ambient pressure and temperature are 101.3 kPa and 293.8 ± 2.8 K, respectively. These carefully controlled initial conditions ensure high reproducibility of the experimental results. The flow, illuminated by a DC-regulated light source (DCR III, SCHOTT North America, Inc.), is captured using a high-speed video camera (FASTCAM SA5, Photron Limited) equipped with schlieren photography. The high-speed camera operates at a frame rate of 60 000 f.p.s. with a shutter time of 1 µs.

Since the incident shock is weak, during most of the experimental period, the post-shock flow can be treated as incompressible (particular after the shock wave departs from the interface) and laminar (except during the later stages following reshock). Consequently, the thickness of the boundary layer in the post-shock flow (Kundu, Cohen & Dowling 2012) can be estimated as follows:

$$\delta^* = 1.72\sqrt{\frac{\mu x}{\rho \Delta V}}, \tag{2.2}$$

where $x \approx 120.0$ mm represents the maximum distance travelled by the interface during the experimental period. Under the experimental temperature and pressure conditions, the viscosity coefficient and the density of air (SF_6) are $\mu = 1.83 \times 10^{-5}$ Pa·s ($= 1.60 \times 10^{-5}$ Pa s) and $\rho = 1.204$ kg m^{-3} ($= 6.143$ kg m^{-3}), respectively. The velocity of the post-shock flow is $\Delta V = 106.2$ m s^{-1}. According to (2.2), the maximum thickness of the boundary layer in the post-shock air (SF_6) flow is calculated to be approximately 0.23 mm (0.09 mm). This value is much smaller than the inner height of the test section (6.0 mm), indicating that the boundary layer has a negligible influence on the interface development during the experimental period. Note that the post-shock flow Mach number in air (reflection side) and SF_6 (transmission side) are 0.27 an 0.73, respectively. While the Mach number in SF_6 exceeds the conventional incompressible threshold, the interface evolves smoothly without signs of compressibility-related effects. Moreover, previous experiments on RMI at classical single-mode air/SF_6 interfaces under similar initial conditions (Liu *et al.* 2018) demonstrated excellent agreement with predictions from incompressible

https://doi.org/10.1017/jfm.2025.10377 Published online by Cambridge University Press

models, further supporting this approximation. Also, previous numerical studies (Ding *et al.* 2017*a*; Li *et al.* 2022*a*) have successfully reproduced experimental results using inviscid Euler solvers, suggesting that boundary-layer effects are not dominant within the temporal and spatial scales of interest. Nevertheless, after the passage of the reflected shock, the boundary layer may become more chaotic or even transition to turbulence. One noticeable effect is an increased interface thickness following reshock. The interaction between reflected shock waves and boundary layers generates additional vorticity that would influence instability growth, particularly during the reshock phase (Balakumar *et al.* 2008; Mohaghar *et al.* 2019; Ferguson & Jacobs 2024*b*). A more complete understanding of reshocked RMI requires a quantitative comparison between vorticity deposited by boundary-layer interaction and that arising from shock-interface interaction. Such analysis necessitates advanced diagnostics, such as particle image velocimetry (PIV) applied perpendicular to the current field of view, as demonstrated in recent work by Ferguson & Jacobs (2024), who highlighted its strong potential in capturing boundary-layer-induced vorticity. However, in our experiments, the application of PIV has proven challenging due to intense light scattering from residual soap-film droplets, yielding unreliable velocity data. Nevertheless, schlieren images still reveal that vorticity generated by shock–boundary-layer interaction enhances flow three-dimensionality, as evidenced by significant interface thickening observed after reshock. Since our current analysis focuses on evolution of the largest flow structures (i.e. the interface width) during the short period following reshock, we believe the influence of additional vorticity is limited. To mitigate boundary-layer influences in our current analysis, the post-shock amplitude is measured at the centre of the interface region, between the tips of spike and bubble, which minimises sensitivity to boundary-layer-induced vertical distortions. To overcome current limitations in flow diagnostics, we are developing a membrane-free interface generation technique using an automatically retractable plate. By eliminating soap droplets and uncontrolled diffusion layers, this method enables the formation of a sharp, membraneless interface with controllable long-wavelength perturbations. It has recently been successfully applied to planar laser-induced fluorescence measurements in converging shock-driven turbulence (Zhao *et al.* 2025). In the near future, we aim to extend the technique to PIV measurements to directly quantify wall-induced vorticity.

The mass fraction of SF_6 on the right side of the interface is estimated using the following method. As a planar shock collides with a flat light/heavy interface, the resulting flow is composed of four uniform regions delineated by a reflected shock, a transmitted shock and the interface. According to one-dimensional gas dynamics theory, we can establish definite relations between the flow parameters on both sides of the reflected and transmitted shocks. Additionally, a compatibility condition exists across the interface, ensuring the continuity of velocity and pressure. Using these relationships, the following equation can be derived:

$$\left[\frac{(\Lambda_2-1)\,\rho_1}{(\Lambda_1-1)\,\rho_2}\right]^{1/2}\frac{P_t-1}{(P_t\Lambda_2+1)^{1/2}}=\frac{P_i-1}{(P_i\Lambda_1+1)^{1/2}}-\left(\frac{\rho_1}{\rho_1'}\right)^{1/2}\frac{P_t-P_i}{(P_t\Lambda_1+P_i)^{1/2}},\tag{2.3}$$

where

$$\left.\begin{aligned}\Lambda_1&=(\gamma_1+1)/(\gamma_1-1)\\ \Lambda_2&=(\gamma_2+1)/(\gamma_2-1)\\ P_i&=1+2\gamma_1/(\gamma_1+1)\left(M_i^2-1\right)\\ \rho_1/\rho_1'&=\left[(\gamma_1-1)M_i^2+2\right]/\left[(\gamma_1+1)M_i^2\right]\end{aligned}\right\}.\tag{2.4}$$

https://doi.org/10.1017/jfm.2025.10377 Published online by Cambridge University Press

Here, γ_1 and ρ_1 represent the specific heat ratio and density on the side of the interface where the incident shock is initially located, while γ_2 and ρ_2 denote the specific heat ratio and the density on the other side, P_i (P_t) refers to the pressure ratio across the incident shock (transmitted shock), ρ_1' to the fluid density behind the incident shock and M_i to the Mach number of the incident shock. In experiment, the gas on the left side of the interface is pure air. The velocity of the incident shock is measured to be $446.6 \pm 7.8\ \mathrm{m\,s^{-1}}$, corresponding to $M_i = 1.30 \pm 0.02$. Given the measured speeds of the incident and transmitted shocks, the mass fraction of SF_6 can be calculated using an iterative method. Specifically, specifying an arbitrary initial value between 0 and 1 for the mass fraction of SF_6 on the right side of the interface, the flow parameters on that side (such as ρ_2 and γ_2) can be determined. Substituting these parameters into (2.3), the pressure ratio across the transmitted shock (P_t) can be solved, providing the strength of the transmitted shock. If the calculated Mach number of the transmitted shock exceeds the measured value, the mass fraction is slightly reduced; conversely, if the calculated Mach number is lower, the mass fraction is increased. This iterative process continues until the calculated Mach number closely matches the measured one, with a difference of less than 0.1 %. The accuracy of this concentration calculation method has been thoroughly validated in recent studies (Zhang *et al.* 2023*a*,b). It is worth noting that the shock impact can cause the soap film to atomise into small droplets, which are subsequently entrained in the flow. The relationship between the size of the soap droplets and the incident shock strength has been investigated by Cohen (1991) and Ranjan *et al.* (2008). According to their work, the mean radius of the soap droplets is estimated to be approximately 30 μm for the shock wave of Ma $\sim$ 1.3 in the present experiments. These micron-sized droplets absorb negligible energy from the shock wave and exert minimal influence on the interface evolution. A series of previous studies (Ranjan *et al.* 2011; Wang, Si & Luo 2013; Ding *et al.* 2017*a*,*b*; Liu *et al.* 2018) on RMI adopting such a soap-film technique have reported good agreement with theoretical and numerical results, confirming the negligible influence of soap droplets during the experimental time scale.

3. The RMI at a single-mode interface with reshock

As a basic problem, the reshocked RMI at a single-mode interface is first investigated. To explore the dependence of instability growth on initial conditions, both the amplitude of the initial interface and the reflection distance (defined as the distance between the initial interface and the inserted block) are varied. In this study, two reflection distances are considered: 40 and 80 mm, referred to as the short (S) and long (L) reflection distances, respectively. Detailed parameters corresponding to the initial conditions for each case are listed in table 1. The notation for each case comprises three components: the first indicates the total number of constituent modes, the second specifies the wavelength and the third denotes the reflection distance. For example, in case M1-60-S, the initial perturbation consists of a single mode (M1) with a wavelength of 60 mm, and the reflection distance is short (40 mm). Note in case M1-60-L^+, a significantly larger reflection distance of 160 mm is used to ensure that the interface reaches the nonlinear stage by the time the reshock occurs.

Sequences of schlieren images illustrating the evolutions of wave pattern and interface morphology for typical cases are displayed in figure 3. Here, we take case M1-40-L as an example to detail the evolution process. In this work, the time origin is defined as the moment when the incident shock reaches the mean position of the initial perturbed interface (i.e. the position of an unperturbed interface). At the beginning (-13 μs), an incident shock (IS), together with an initial interface (II), is clearly discerned. After the IS passes across the II, it splits immediately into an upstream-moving reflected

https://doi.org/10.1017/jfm.2025.10377 Published online by Cambridge University Press

Case	L (mm)	λ (mm)	ka_r^-	Vfra (SF_6)	ΔV_2 ($m\,s^{-1}$)	A^+	A_r^+	da_1/dt ($m\,s^{-1}$)	da_2/dt ($m\,s^{-1}$)	V_s^{lin} ($m\,s^{-1}$)	V^{lin} ($m\,s^{-1}$)
M1-60-*S*	40	60	0.20	98.9 %	138.1	0.71	−0.73	5.6	7.2	7.2	7.2
M1-40-*S*	40	40	0.38	99.9 %	148.7	0.71	−0.73	8.8	17.1	17.3	17.3
M1-30-*S*	40	30	0.58	91.4 %	136.4	0.69	−0.71	7.1	19.3	30.1	19.5
M1-20-*S*	40	20	1.07	99.2 %	141.3	0.71	−0.73	8.1	28.2	62.8	28.6
M1-60-*L*	80	60	0.34	98.9 %	138.1	0.71	−0.73	5.7	16.0	16.3	16.3
M1-40-*L*	80	40	0.63	90.4 %	136.0	0.69	−0.71	2.7	23.9	37.1	24.7
M1-30-*L*	80	30	1.02	91.4 %	136.4	0.69	−0.71	5.4	28.1	59.3	28.9
M1-20-*L*	80	20	1.39	99.4 %	142.5	0.71	−0.73	4.4	28.7	88.0	35.6
M1-30-L^+	160	30	1.38	96.8 %	147.3	0.71	−0.73	2.8	22.6	93.5	36.0

Table 1. Detailed parameters corresponding to the initial conditions for each case. Here, L refers to the distance between the interface and the end wall, λ to the wavelength, ka_r^- to the product of the wavenumber and pre-reshock amplitude, Vfra(SF_6) to the volume fraction of SF_6 on the right side of the interface, ΔV_2 to the interface velocity jump caused by reshock, A^+ and A_r^+ to the post-shock and post-reshock Atwood numbers, respectively, da_1/dt and da_2/dt stand for the pre-reshock and post-reshock growth rates, respectively, V_s^{lin} is the linear growth rate predicted by (3.2) and V^{lin} is post-reshock growth rate calculated with (3.3).

shock (RS_1) and a downstream-moving transmitted shock (TS_1). Afterwards, the shocked interface (SI) moves downstream, presenting a clear and distinct single-mode shape (47 μs). This confirms the reliability of the present experimental methods. Meanwhile, the interface amplitude continues to increase over time, driven by the baroclinic vorticity deposited at the interface during the shock-interface interaction. Later, nonlinearity becomes pronounced and new harmonics are generated, causing the interface to deviate from a sinusoidal shape. Subsequently, the transmitted shock TS_1 propagates forward and collides with the inserted block, generating a reflected transmitted shock (RTS, 567 μs). At 627 μs, the RTS interacts with the deforming interface, bifurcating into a second transmitted shock (TS_2) and a reflected rarefaction wave (RW_1). Following this interaction, the interface amplitude suffers a quick decay to zero by 727 μs, a phenomenon known as phase inversion, and subsequently increases with an opposite phase. As time proceeds, the rarefaction wave RW_1 propagates toward the end wall of the shock tube. Upon reaching the wall, this wave returns as a secondary rarefaction wave, which subsequently re-accelerates the interface. The resulting wave pattern continues to reflect back and forth between the wall and the interface, thereby influencing the instability evolution. To address this concern, we have plotted x–t diagrams to show the evolution of the interface and wave patterns under different reflection distances, as shown in figure 4. It is clearly shown that increasing the distance between the interface and the end wall leads to a longer interface evolution period prior to the arrival of the reflected rarefaction wave (denoted as RRW_1). It is important to note that the post-reshock growth rates reported hereinafter are extracted from the interface evolution before the reflected rarefaction wave arrives. Therefore, the observed growth behaviour can be attributed solely to reshock effects and is not influenced by subsequent wave reflections.

Previous studies have shown that, following reshock, the interface amplitude increases with time in a quasi-linear manner. Recent experiments by Zhang *et al.* (2023*b*) demonstrated that the linear superposition model, originally proposed by Mikaelian (1985), can effectively predict the post-reshock growth rate, provided that the instability evolution remains within the linear regime prior to reshock. The model is expressed as

$$\frac{da_2}{dt} = ka_r^+ A_r^+ \Delta V_2 - \frac{da_1}{dt}, \tag{3.1}$$

https://doi.org/10.1017/jfm.2025.10377 Published online by Cambridge University Press

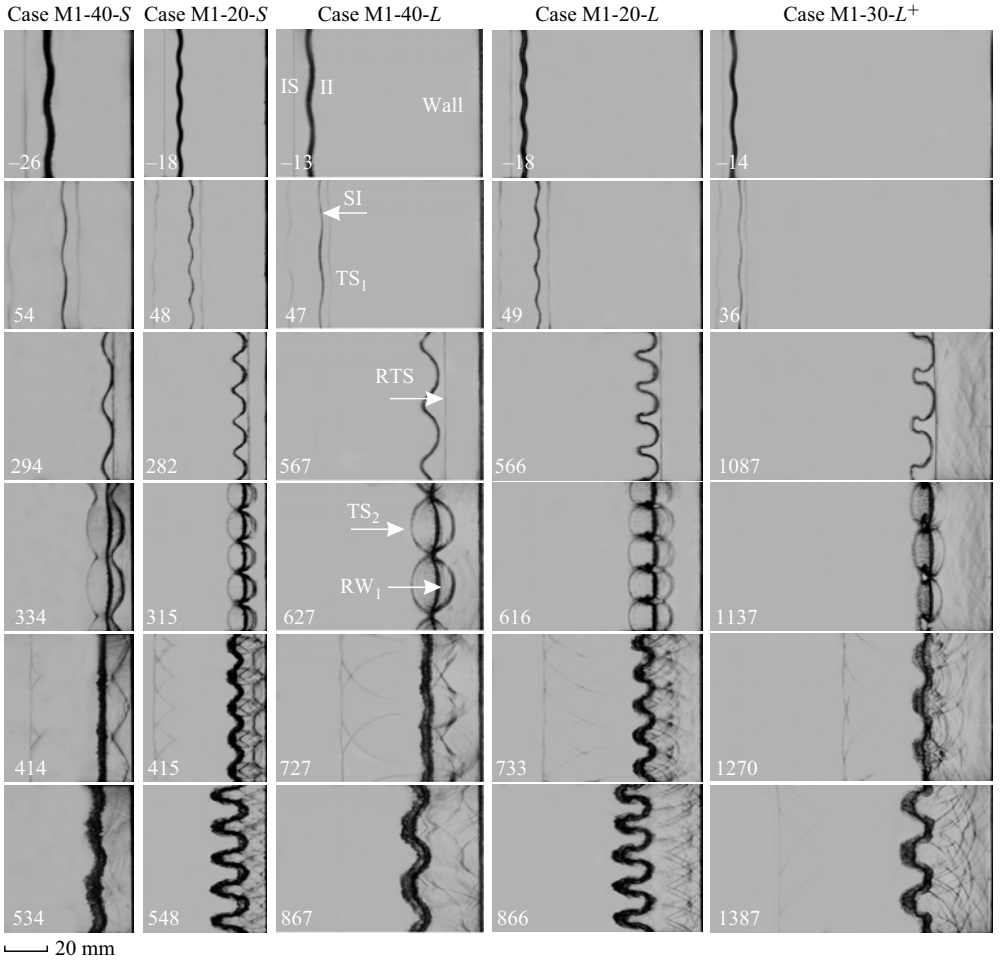


Figure 3. Sequences of schlieren images illustrating the instability growth for various single-mode cases: IS, incident shock; II, initial interface; SI, shocked interface; TS_1, the first transmitted shock; TS_2, the second transmitted shock; RTS, reflected transmitted shock; RW_1, the first rarefaction wave. The numbers are in μs.

where a_r^+ refers to the post-reshock amplitude of the interface, ΔV_2 to the velocity jump of the interface caused by reshock and A_r^+ to the post-reshock Atwood number. The subscripts 1 and 2 denote the stages before and after reshock, respectively. The original model of Mikaelian (1985) is applicable only to light/heavy interfaces. To extend its applicability to heavy/light interfaces, based on the work of Vandenboomgaerde, Mügler & Gauthier (1998) and Zhang *et al.* (2023*b*) proposed a modified version

$$\frac{\mathrm{d}a_2}{\mathrm{d}t} = k\Delta V_2 \left(\frac{A_r^+ a_r^+ + A_r^- a_r^-}{2} \right) - \frac{\mathrm{d}a_1}{\mathrm{d}t}, \tag{3.2}$$

where the superscripts '−' and '+' denote the moments just before and after reshock, respectively. As shown in table 1, (3.2) usefully predicts the post-reshock growth rate for small-amplitude cases, where $ka_r^- < 0.38$. However, as the amplitude-to-wavelength ratio become larger at the time of reshock, the model tends to overestimate the post-reshock growth rate. Building on several earlier studies (Dimonte & Ramaprabhu 2010; Buttler *et al.* 2012; Probyn *et al.* 2021), Guo *et al.* (2022*b*) attributed this overestimation primarily

https://doi.org/10.1017/jfm.2025.10377 Published online by Cambridge University Press

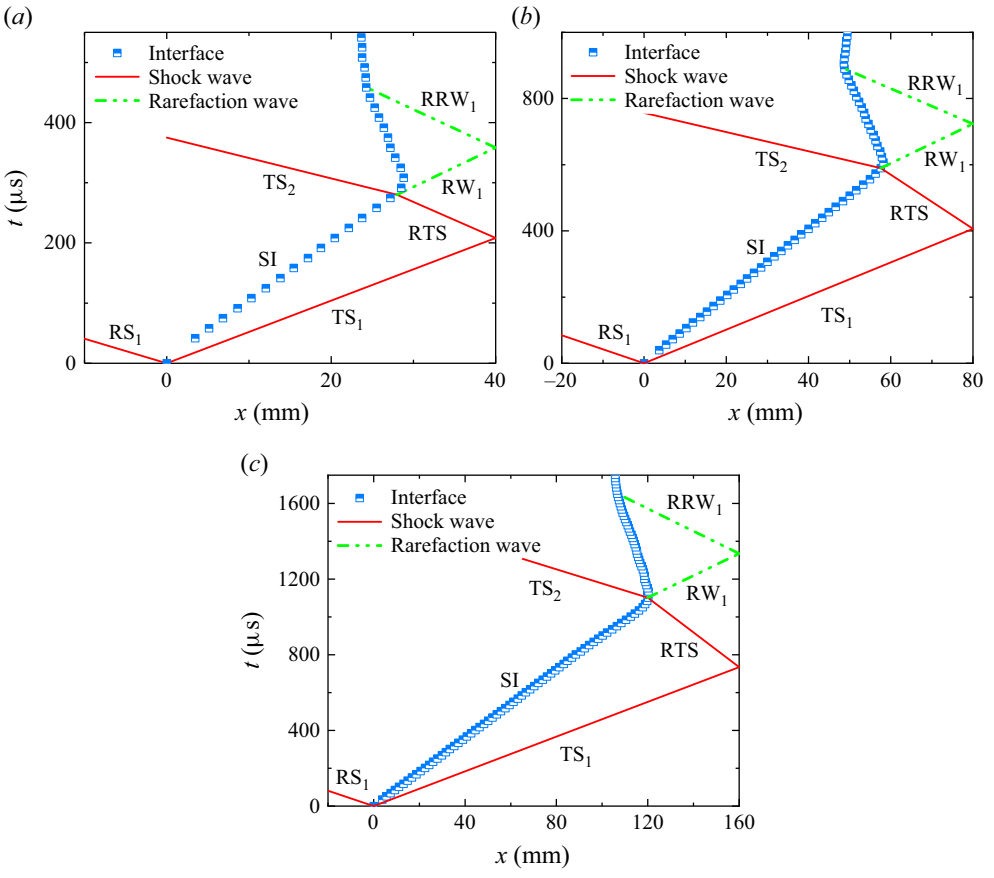


Figure 4. An x–t diagram showing the trajectories of the interface and waves for different reflection distances (*a*) 40 mm, (*b*) 80 mm and (*c*) 160 mm.

to the large-amplitude effect, which is not accounted for in the model. To address this issue, we incorporate a correction factor R^{Guo} into (3.2), as suggested by Guo *et al.* (2022*b*), to account for the large-amplitude effect. The revised model is expressed as follows:

$$\frac{\mathrm{d}a_2}{\mathrm{d}t} = R^{Guo} k \Delta V_2 \left(\frac{A_r^+ a_r^+ + A_r^- a_r^-}{2} \right) - \frac{\mathrm{d}a_1}{\mathrm{d}t}, \tag{3.3}$$

where

$$R^{Guo} = \begin{cases} 1 & (ka_r^- < 0.38) \\ \dfrac{1}{1.2 + (ka_r^-)^2/1.5} & (ka_r^- \geqslant 0.38) \end{cases}. \tag{3.4}$$

Note that the current formulation of the correction factor in (3.3) is not mathematically continuous at $ka_r^- = 0.38$. The correction factor for $ka_r^- \geqslant 0.38$ is empirically fitted based on experimental data and prior insights. For $ka_r^- < 0.38$, due to limited experimental resolution and lack of detailed data, a constant correction factor of 1 is applied here. This highlights the need for future investigations into the transitional ka_r^- regime though additional experiments to refine the discontinuity. Despite this, as shown in table 1, (3.3) provides significantly improved predictions compared with the original model, particularly for large-amplitude cases.

https://doi.org/10.1017/jfm.2025.10377 Published online by Cambridge University Press

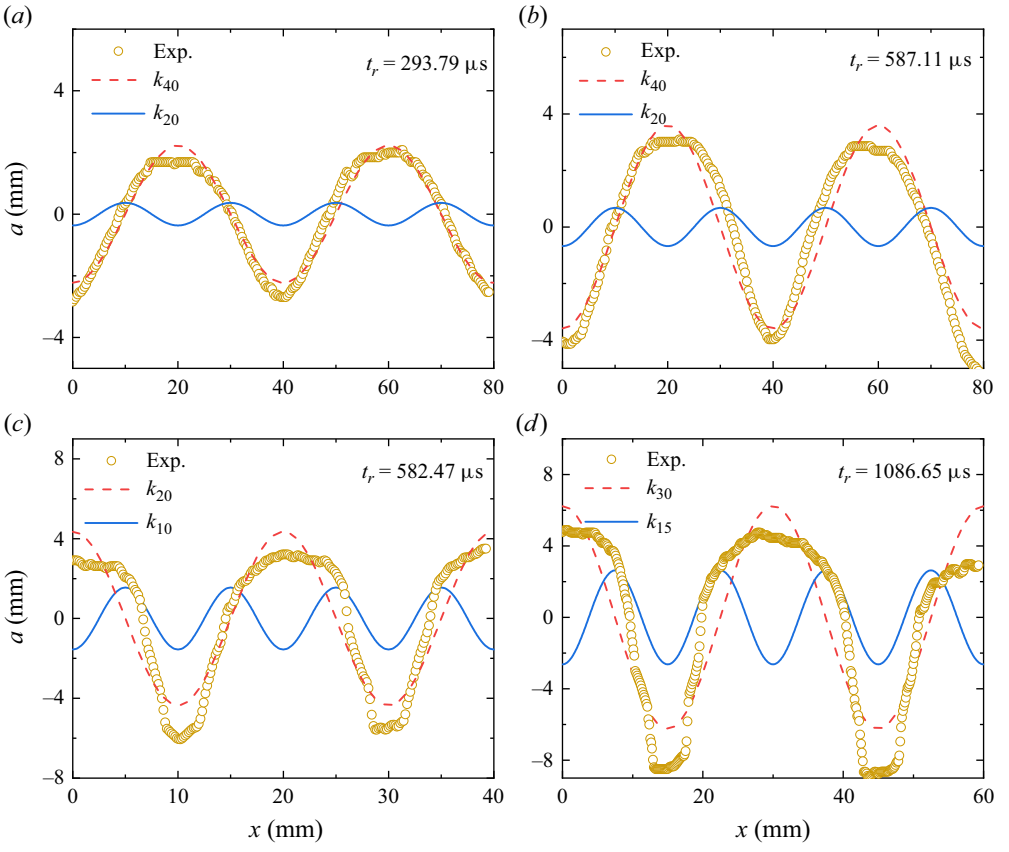


Figure 5. Morphologies of the whole interface extracted from schlieren images and the basic modes obtained with Fourier analysis at the time of reshock for (*a*) case M1-40-*S*, (*b*) case M1-40-*L*, (*c*) case M1-20-*L* and (*d*) case M1-30-L^+.

As the amplitude-to-wavelength ratio increases further (e.g. cases M1-20-*L* and M1-30-L^+), (3.3) fails to provide accurate predictions. Notably, cases M1-20-*L* and M1-30-L^+ share identical ka_r^- values, implying that they should exhibit similar growth rates according to the model. However, experimental measurements reveal significant differences in their growth rates, highlighting a limitation of the revised model in predicting reshocked RMI at large-amplitude interfaces. This discrepancy suggests that current models may overlook crucial physical mechanisms in large-amplitude cases. Our limited understanding of reshocked RMI mechanisms, particularly in the nonlinear regime, impedes the identification and incorporation of these missing factors into theoretical models.

As illustrated in figure 3, when either the reflection distance or the initial amplitude-to-wavelength ratio increases, the interface no longer maintains a single-mode shape upon the arrival of the reflected shock. An image-processing program is utilised to extract the interface morphology from schlieren images. By performing Fourier decomposition on the extracted morphologies, the amplitudes of harmonics at the time of reshock are available, as plotted in figure 5. It is observed that as ka_r^- increases, higher harmonics become more pronounced. Although cases M1-30-L^+ and M1-20-*L* share the same amplitude-to-wavelength ratio prior to reshock, the former exhibits more significant harmonics (indicating stronger nonlinearity) than the latter. We realise that the lower post-reshock

https://doi.org/10.1017/jfm.2025.10377 Published online by Cambridge University Press

Case	L (mm)	λ_k (mm)	λ_{2k} (mm)	ϕ_k	ϕ_{2k}	Vfra (SF_6)	ΔV_2 (m s^{-1})	A^+	A_r^+
M2-0-S	40	40	20	0	0	98.4 %	139.5	0.71	0.73
M2-π-S	40	40	20	0	π	88.1 %	144.3	0.68	0.71
M2-0-L	80	40	20	0	0	85.5 %	129.0	0.70	0.72
M2-π-L	80	40	20	0	π	94.2 %	135.6	0.70	0.72

Table 2. Detailed parameters corresponding to the initial conditions for dual-mode cases. Here, L refers to the distance from the interface to the end wall, λ to the wavelength, ϕ to the perturbation phase, Vfra(SF_6) to the volume fraction of SF_6 on the right side of the interface, ΔV_2 to the velocity jump of the interface caused by reshock and A^+ and A_r^+ to the post-shock and post-reshock Atwood numbers, respectively.

growth rate in case M1-30-L^+ may be attributed to the stronger coupling effect between the fundamental mode and the second (even higher) harmonic, a factor not accounted for in existing models. To validate this hypothesis, experiments on the reshocked RMI at dual- and triple-mode interfaces, which involves stronger nonlinearity, are desired.

4. The RMI at a dual-mode interface with reshock

In this section, the reshocked RMIs at four types of dual-mode interfaces, which possess various mode compositions and phase differences, are examined. The phase of the second mode relative to the first one is set to be either 0 or π, corresponding to in-phase and anti-phase cases, respectively. Detailed parameters corresponding to the initial conditions for each case are listed in table 2. Developments of the interface morphologies and wave patterns for the dual-mode cases are displayed in figure 6. Unlike the single-mode case, the dual-mode interface exhibits asymmetry at the beginning. The mixing width, defined as the maximum distance between the spike and bubble tips (i.e. $h = 2a$), can be accurately measured from schlieren images. As the reflection distance increases, the shock-accelerated interface experiences a longer evolution period between the initial shock passage and reshock arrival, resulting in a larger mixing width prior to reshock. Additionally, the roll-up of the spike becomes more pronounced, indicating stronger nonlinearity compared with the single-mode case. This is consistent with the previous findings on multi-mode RTI (Ofer *et al.* 1996).

A distinct feature of dual-mode RMI is its reduced periodicity along the transverse direction compared with the single-mode case. Specifically, in case M2-0-L, after the shock impact, the larger bubble grows significantly faster than the smaller ones, i.e. the absolute growth rate of the larger bubble is higher than that of the smaller one. As time progresses, the larger bubble gradually encroaches on the adjacent smaller ones, and, consequently, the spikes develop with an apparent inclination to the large bubble (519 μs). For case M2-π-L with anti-phase perturbations, all bubbles initially have the same shape and size, evolving symmetrically over time. The spikes, despite having two different initial sizes, also exhibit symmetric evolution. Eventually, the larger spike rolls up noticeably, similar to that seen in single-mode RMI, while the growth of the smaller spike is significantly suppressed, leading to the absence of roll-up structures. Furthermore, it is observed that this non-periodic characteristic of the interface structure persists even after the reshock impact. Following reshock, the interface undergoes phase inversion (i.e. spikes transform into bubbles and *vice versa*) due to the deposition of reverse vorticity. Although the post-inversion interface structure remains asymmetric, the amplitude differences between spikes and between bubbles are significantly reduced. For

https://doi.org/10.1017/jfm.2025.10377 Published online by Cambridge University Press

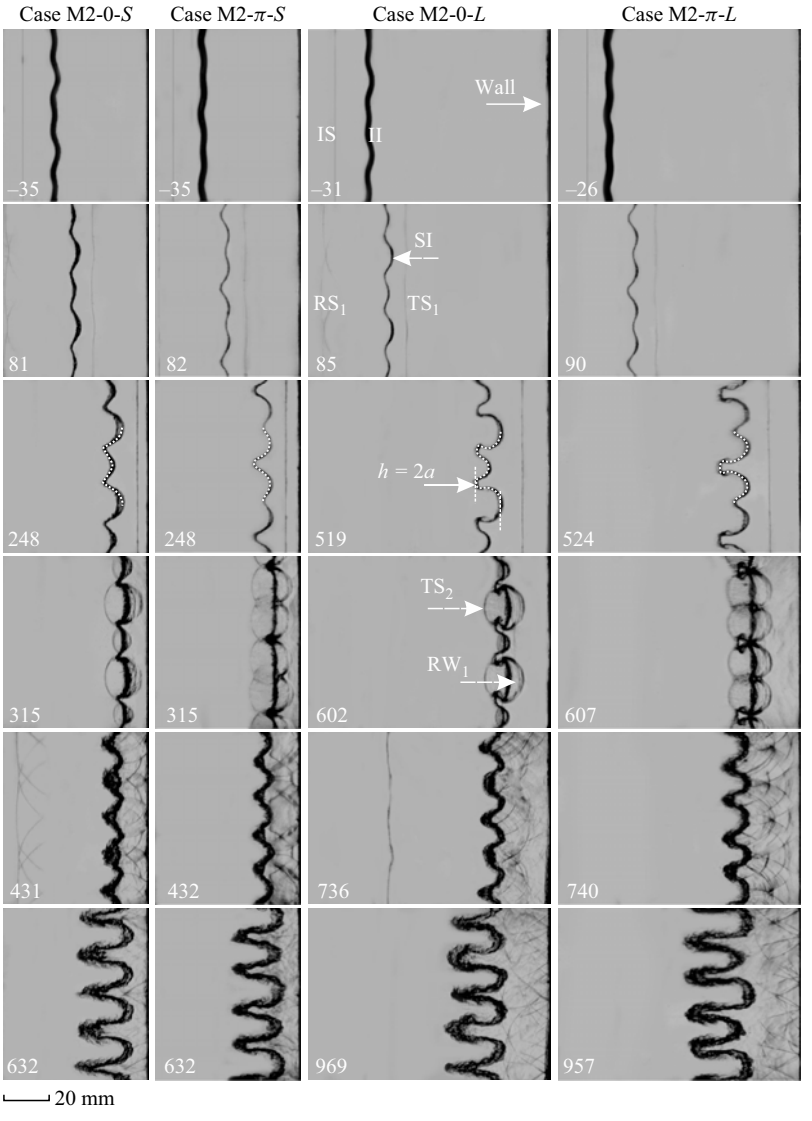


Figure 6. Sequences of schlieren images for various dual-mode cases. The unit of numbers is μs. The symbols are the same as those in figure 3.

case M2-0-*L*, prior to reshock (519 μs), the interface exhibits two large bubbles alongside three smaller ones. After phase inversion (736 μs), while morphological distinctions persist, the amplitude differences among the inverted structures are notably diminished. Specifically, the previously larger bubbles develop into smaller, flat-topped spikes, while the smaller bubbles evolve into larger, sharp-topped spikes. This characteristic phase inversion behaviour is observed across all experimental cases. As the reflection distance increases, this non-periodicity becomes more pronounced. The present results manifest the evident dependence of reshocked RMI on initial perturbation spectra. Despite this, it is important to note that this sensitivity diminishes after reshock.

Previous experiments on reshocked RMI at random multi-mode interfaces have shown that the impact of the reflected shock can cause a rapid transition to turbulent mixing

https://doi.org/10.1017/jfm.2025.10377 Published online by Cambridge University Press

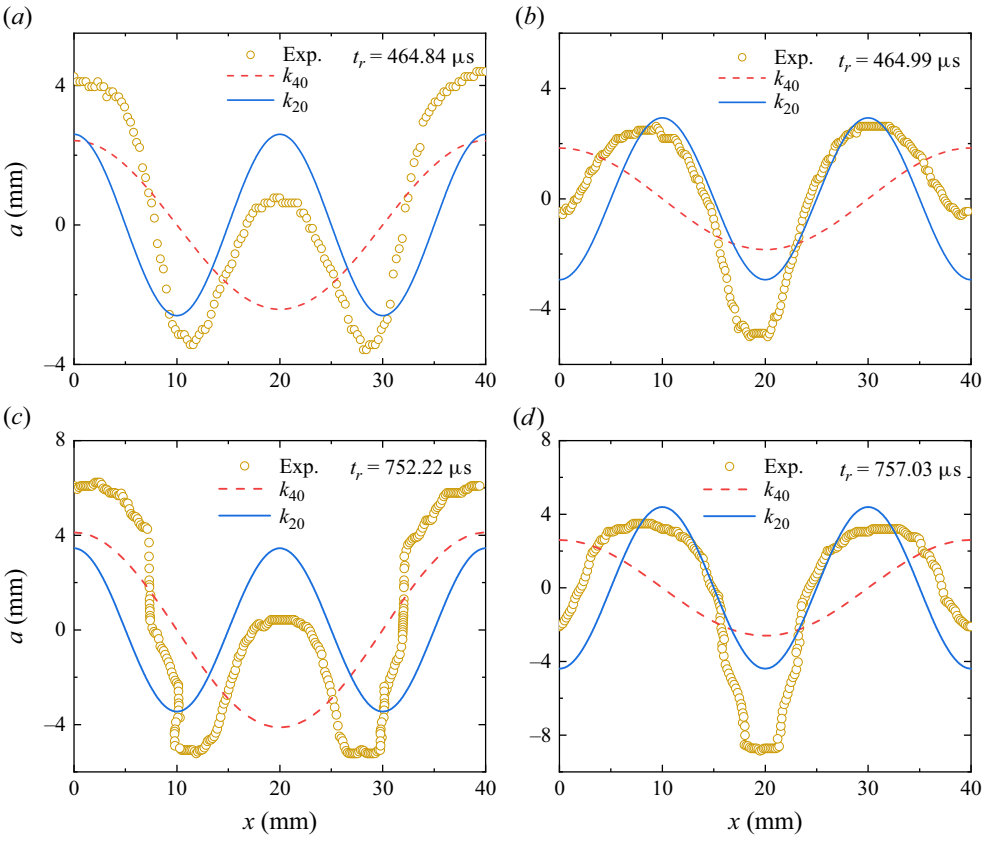


Figure 7. Morghologies of the whole interface extracted from schlieren images and the basic modes obtained with Fourier analysis at the time of reshock for (*a*) case M2-0-*S*, (*b*) case M2-π-*S*, (*c*) case M2-0-*L* and (*d*) M2-π-*L*.

(Leinov *et al.* 2009). In those experiments, characterising the perturbation spectrum at initial multi-mode interfaces is challenging, hindering flow decomposition. In the present experiment, the clear and distinct interface contours extracted from the high-fidelity schlieren images enable us to conduct Fourier analysis, thereby facilitating the analysis on the generation and growth of harmonics, as shown in figure 7. Here, the interface contours extracted from schlieren images are represented by the hollow circles, while the harmonics obtained through Fourier analysis are depicted by lines. Note the interface contours are extracted from the central region of the schlieren images, as indicated by the white dashed lines in figure 6, effectively minimising the influence of the sidewall. Notably, the mixing width at the time of reshock remains invariant across all cases. In all cases, the second harmonic exhibits a considerably large amplitude, demonstrating evident nonlinear behaviour in dual-mode cases. As shown in § 3, for an initial single-mode interface, the instability growth after reshock is still dominated by the fundamental mode of the initial interface. However, for dual-mode cases, the coupling between the harmonics and basic modes would play a significant role in instability growth. Previous studies have shown that for interfaces with a dominant mode before reshock, the post-reshock growth rate exhibits only a very weak correlation with ka_r^- (Charakhch'An 2000; Ukai, Balakrishnan & Menon 2011). Furthermore, for interfaces with random multi-mode perturbations, the post-reshock growth rate is almost independent of ka_r^- (Leinov *et al.* 2009). These

https://doi.org/10.1017/jfm.2025.10377 Published online by Cambridge University Press

observations may be attributed to mode-coupling effects. The high-fidelity experimental results obtained here enable us to perform a detailed analysis on the harmonic growth such that a more in-depth understanding of the regimes of reshocked RMI can be gained.

Under the assumptions of incompressible, irrotational and inviscid flow, Haan (1991) developed a modal model for the RTI at a three-dimensional multi-mode interface using the perturbation expansion method. This model incorporates mode-coupling effects and is expressed as

$$\ddot{a}_k = \gamma(k)^2 a_k + kA \sum_{k'} \left\{ \ddot{a}_{k'} a_{k-k'} \left(1 - \hat{\boldsymbol{k}}' \cdot \hat{\boldsymbol{k}}\right) + \dot{a}_{k'} \dot{a}_{k-k'} \left[\frac{1}{2} - \hat{\boldsymbol{k}}' \cdot \hat{\boldsymbol{k}} - \frac{1}{2} \hat{\boldsymbol{k}}' \cdot \left(\hat{\boldsymbol{k}} - \hat{\boldsymbol{k}}'\right) \right] \right\}, \tag{4.1}$$

where $\gamma(k)^2 a_k$ is the linear growth rate and $\hat{\boldsymbol{k}}$ is the unit vector $\boldsymbol{k}/k$. In the case of two-dimensional perturbations, Ofer *et al.* (1996) derived a second-order analytical solution for the growth of perturbation amplitude with time

$$a_k(t) = a_k^{lin}(t) + \frac{1}{2} kA \left(\sum_{k'} a_{k'}^{lin}(t) a_{k+k'}^{lin}(t) - \frac{1}{2} \sum_{k'<k} a_{k'}^{lin}(t) a_{k-k'}^{lin}(t) \right). \tag{4.2}$$

Luo *et al.* (2020) and Chen *et al.* (2024) have applied this model to predict RMI at perturbed interfaces under a single shock. To quantify the mode-coupling effects in reshocked RMI, we follow the approach of Luo *et al.* (2020) and Chen *et al.* (2024) by taking the second-order time derivative of (4.2)

$$\ddot{a}_k(t) = \ddot{a}_k^{lin}(t) + \frac{1}{2} kA \left[\sum_{k'} (\ddot{a}_{k'}^{lin}(t) a_{k+k'}^{lin}(t) + 2\dot{a}_{k'}^{lin}(t) \dot{a}_{k+k'}^{lin}(t) + a_{k'}^{lin}(t) \ddot{a}_{k+k'}^{lin}(t)) - \frac{1}{2} \sum_{k'<k} (\ddot{a}_{k'}^{lin}(t) a_{k-k'}^{lin}(t) + 2\dot{a}_{k'}^{lin}(t) \dot{a}_{k-k'}^{lin}(t) + a_{k'}^{lin}(t) \ddot{a}_{k-k'}^{lin}(t)) \right]. \tag{4.3}$$

Chen *et al.* (2024) simplified (4.3) by replacing the term $2\dot{a}_{k'}^{lin}(t)\dot{a}_{k+k'}^{lin}(t)$ with linear growth rates measured from RMI experiments. Time integration of the modified equation yields a growth rate that contains a temporal term $2V_{k'}^{lin} V_{k+k'}^{lin} t$, suggesting that mode-coupling effects evolve with time. While this approach has been validated for single-shock impacts on small-amplitude interfaces, its application to reshocked RMI presents significant challenges. For reshock cases, interfaces develop larger amplitudes and higher growth rates, causing the term $2V_{k'}^{lin} V_{k+k'}^{lin} t$ to exhibit strong temporal dependence, significantly influencing the growth rate evolution. However, as shown in figure 12(*b*), the interface exhibits an almost linear growth following reshock, indicating low sensitivity to time. This discrepancy suggests that the conventional derivations fail to capture the fundamental physics of reshocked RMI. This inconsistency motivates our development of a new time-independent modal model specifically for reshock conditions.

It is important to note that Richtmyer's impulsive model (Richtmyer 1960) is naturally an extension of the linear theory of RTI for the case of a single-mode interface. In his seminar work, Richtmyer approximated the shock impact as a delta-function-like impulse, leading to a simplified impulsive model for the post-shock interface evolution. In this work, we adopt a similar approach for the multi-mode case. Specifically, we starts from the well-established weakly nonlinear RTI framework formulated by Haan (1991), and

https://doi.org/10.1017/jfm.2025.10377 Published online by Cambridge University Press

then introduce the impulsive acceleration (i.e. Dirac delta function) to represent the shock impact. This yields a weakly nonlinear model for early-time multi-mode RMI. Specifically, substituting the initial conditions below for RTI flows into the above equation

$$a(t) = e^{\sqrt{kAg}t},\ \dot{a}(t) = \sqrt{kAg}a(t),\ \ddot{a}(t) = kAga(t), \tag{4.4}$$

we obtain

$$\begin{aligned}\ddot{a}_k(t) = kAga_k^{lin}(t) + \frac{1}{2}kA\Bigg\{&\sum_{k'}\Big[k'Aga_{k'}^{lin}(t)a_{k+k'}^{lin}(t) + 2\sqrt{k'(k+k')}Aga_{k'}^{lin}(t)a_{k+k'}^{lin}(t)\\ &+(k+k')Aga_{k+k'}^{lin}(t)a_{k'}^{lin}(t)\Big]\\ -\frac{1}{2}&\sum_{k'<k}\Big[k'Aga_{k'}^{lin}(t)a_{k-k'}^{lin}(t) + 2\sqrt{k'(k-k')}Aga_{k'}^{lin}(t)a_{k-k'}^{lin}(t)\\ &+(k-k')Aga_{k-k'}^{lin}(t)a_{k'}^{lin}(t)\Big]\Bigg\}.\end{aligned} \tag{4.5}$$

This expression incorporates both linear growth terms and nonlinear mode-coupling terms, as indicated by the summation over different wavenumbers. For the RMI, the acceleration can be modelled as an impulsive function

$$g = \Delta v\delta(t), \quad \delta(t) = \begin{cases}0 & (t \neq 0)\\ 1 & (t = 0)\end{cases}. \tag{4.6}$$

By substituting (4.6) into (4.5) and integrating the resulting expression with respect to time, an analytical solution that accounts for mode-coupling effects is obtained, enabling the calculation of the growth rate of mode k for RMI. The solution is expressed as

$$\begin{aligned}V_k^M = V_k^{lin} + \frac{1}{2}Ak\Bigg\{&\sum_{k'}\left[\left(1+\sqrt{\frac{k+k'}{k'}}\right)V_{k'}^{lin}a_{k+k'}^{+} + \left(1+\sqrt{\frac{k'}{k+k'}}\right)V_{k+k'}^{lin}a_{k'}^{+}\right]\\ -\frac{1}{2}&\sum_{k'<k}\left[\left(1+\sqrt{\frac{k-k'}{k'}}\right)V_{k'}^{lin}a_{k-k'}^{+} + \left(1+\sqrt{\frac{k'}{k-k'}}\right)V_{k-k'}^{lin}a_{k'}^{+}\right]\Bigg\}.\end{aligned} \tag{4.7}$$

Here, V_k^{lin} is the linear growth rate of mode k calculated using (3.3) and a_k^+ denotes the post-shock amplitude. Equation (4.7) yields a time-independent coupled growth rate, consistent with the present experimental observations.

Fourier analysis of the extracted interface morphologies enables the decomposition of the interface into its constituent modes. This enables us to track the evolution of each harmonic over time and analyse their individual growth rates. Here, we consider the coupling effect among only the first four harmonics on the growth of each fundamental mode. According to (4.7), the growth rates of the basic modes (k and $2k$) following reshock can be calculated as

$$\begin{aligned}V_k^M = V_k^{lin} &+ \frac{1}{2}A_r^+k_1\left[\left(1+\sqrt{2}\right)V_k^{lin}a_{2k}^{+} + \left(1+\frac{\sqrt{2}}{2}\right)V_{2k}^{lin}a_k^{+}\right]\\ &+ \frac{1}{2}A_r^+k_1\left[\left(1+\sqrt{\frac{3}{2}}\right)V_{2k}^{lin}a_{3k}^{+} + \left(1+\sqrt{\frac{2}{3}}\right)V_{3k}^{lin}a_{2k}^{+}\right]\\ &+ \frac{1}{2}A_r^+k_1\left[\left(1+\sqrt{\frac{3}{4}}\right)V_{3k}^{lin}a_{4k}^{+} + \left(1+\sqrt{\frac{3}{4}}\right)V_{4k}^{lin}a_{3k}^{+}\right],\end{aligned} \tag{4.8}$$

https://doi.org/10.1017/jfm.2025.10377 Published online by Cambridge University Press

Case	a_{rk}^0 (mm)	a_{r2k}^0 (mm)	a_{r3k}^+ (mm)	a_{r4k}^+ (mm)	V_{3k}^{lin} ($\mathrm{m\,s^{-1}}$)	V_{4k}^{lin} ($\mathrm{m\,s^{-1}}$)	$\mathrm{d}a_1/\mathrm{d}t_k$ ($\mathrm{m\,s^{-1}}$)	$\mathrm{d}a_1/\mathrm{d}t_{2k}$ ($\mathrm{m\,s^{-1}}$)
M2-0-S	2.42	2.60	0.47	0.11	−1.19	5.49	8.27	3.84
M2-π-S	1.84	2.93	0.20	0.01	−6.48	7.44	4.36	6.74
M2-0-L	4.12	3.45	0.52	0.11	−8.2	5.95	6.27	1.65
M2-π-L	2.60	4.39	0.82	0.70	4.01	5.85	3.97	7.12

Table 3. Detailed parameters corresponding to the initial conditions for dual-mode cases. Here, a_r^0 refers to the interface amplitude at the moment before the reshock, a_r^+ to the interface amplitude at the moment after the reshock, V^{lin} to the post-reshock growth rate of the interface and $\mathrm{d}a_1/\mathrm{d}t$ to the pre-reshock growth rate of the interface. The symbols '+' and '−' indicate whether the phase is in phase with the first-order fundamental mode (+) or out of phase (−).

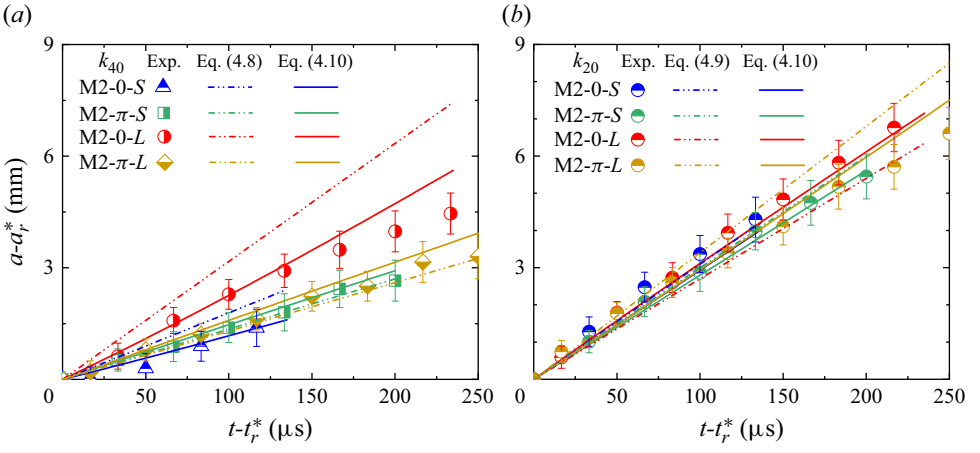


Figure 8. The amplitude growths of modes k (*a*) and $2k$ (*b*) for dual-mode cases following reshock.

$$V_{2k}^{M} = V_{2k}^{lin} - A_r^+ k_2 V_k^{lin} a_k^+ + \frac{1}{2} A_r^+ k_2 \left[\left(1+\sqrt{3}\right) V_k^{lin} a_{3k}^+ + \left(1+\sqrt{\frac{1}{3}}\right) V_{3k}^{lin} a_k^+ \right] + \frac{1}{2} A_r^+ k_2 \left[\left(1+\sqrt{2}\right) V_{2k}^{lin} a_{4k}^+ + \left(1+\frac{\sqrt{2}}{2}\right) V_{4k}^{lin} a_{2k}^+ \right], \tag{4.9}$$

where the amplitude and growth rate of the $3k$ and $4k$ modes after reshock are measured from experiment, as presented in table 3.

As shown in figure 8, the predictions of the modal mode deviate from the experimental results. For instance, in case M2-0-L, a notable discrepancy is observed between the model predictions and experimental data for the k_{40} mode, with smaller deviations also present for other modes. The primary reason for this discrepancy is given below. As can be seen from the present schlieren images, after the reflected shock interacts with the interface, phase inversion occurs and the amplitude growth restarts from near zero. Consequently, in the early stages, the amplitude remains very small, and the effects of mode coupling are negligible. This is consistent with the observation that Haan (1991), who pointed out that, for RMI or RTI at a multi-mode interface, each mode evolves independently within the

https://doi.org/10.1017/jfm.2025.10377 Published online by Cambridge University Press

Case	L (mm)	λ_k (mm)	λ_{2k} (mm)	λ_{3k} (mm)	ϕ_k	ϕ_{2k}	ϕ_{3k}	Vfra (SF_6)	ΔV_2 ($m\,s^{-1}$)	A^+	A_r^+
M3-0-S	40	60	30	20	0	0	0	88.8 %	144.2	0.68	0.70
M3-π-S	40	60	30	20	0	0	π	91.8 %	135.1	0.69	0.72
M3-0-L	80	60	30	20	0	0	0	80.1 %	131.6	0.65	0.67
M3-π-L	80	60	30	20	0	0	π	99.8 %	134.5	0.71	0.73

Table 4. Detailed parameters corresponding to the initial conditions for triple-mode cases. Here, L refers to the distance from the interface to the end wall, λ to the wavelength, ϕ to the perturbation phase, Vfra(SF_6) to the volume fraction of SF_6 on the right side of the interface, ΔV_2 to the interface velocity jump caused by reshock and A^+ and A_r^+ to the post-shock and post-reshock Atwood numbers, respectively.

linear regime. Inspired by the concept of asymptotic matching, we propose an empirical model that matches the initial linear growth rate and the late asymptotic growth rate that accounts for mode-coupling effects. The model is expressed as

$$V^H(t) = \frac{20t + \frac{L}{|V^{\mathrm{M}}|}}{20t + \frac{L}{|V^{lin}|}} V^{\mathrm{M}}, \tag{4.10}$$

where L is the length scale, corresponding to the width of the test section (120 mm in this work). By substituting (4.8) and (4.9) into (4.10), the amplitude growth of each fundamental mode after reshock can be estimated, as given in figure 8. Here, t_r^* denotes the moment at which phase reversion ends and a_r^* is the amplitude at t_r^*. This new model provides reliable predictions for the growth of fundamental modes across all cases examined in this study. To the authors' knowledge, this represents the first modal model developed for reshocked RMI at multi-mode interfaces. Note that (4.10) is physically motivated, as it is constructed to capture the transition from linear to nonlinear growth, although the exact coefficients are empirically calibrated against experimental data. The error bars in figure 8 represent uncertainties associated with the extraction of interface profiles, rather than statistical variations from repeated experiments. These uncertainties primarily arise from experimental limitations, including the spatial resolution of the imaging system, interface broadening caused by fragmented soap-film droplets and three-dimensional effects.

5. The RMI at a triple-mode interface with reshock

To further validate the developed model and explore mode-coupling effects in reshocked RMI in greater depth, four sets of triple-mode interfaces are examined. Similar to the dual-mode case, various reflection distances and phase differences are considered. Detailed parameters for these cases are listed in table 4. The evolutions of interface morphologies and wave patterns for these cases, illustrated by schlieren images, are presented in figure 9. The amplitudes of the fundamental modes and harmonics at the time of reshock, obtained through Fourier decomposition of the extracted interface morphologies, are plotted in figure 10. In this figure, the circle symbols represent the extracted interface contours, while the solid lines depict the fundamental modes obtained through Fourier decomposition. These cases exhibit comparable amplitudes at any given time following reshock.

By incorporating the coupling effects between the first to sixth harmonics on the growth of each fundamental mode, the growth of the three fundamental modes can be described by the following equations:

https://doi.org/10.1017/jfm.2025.10377 Published online by Cambridge University Press

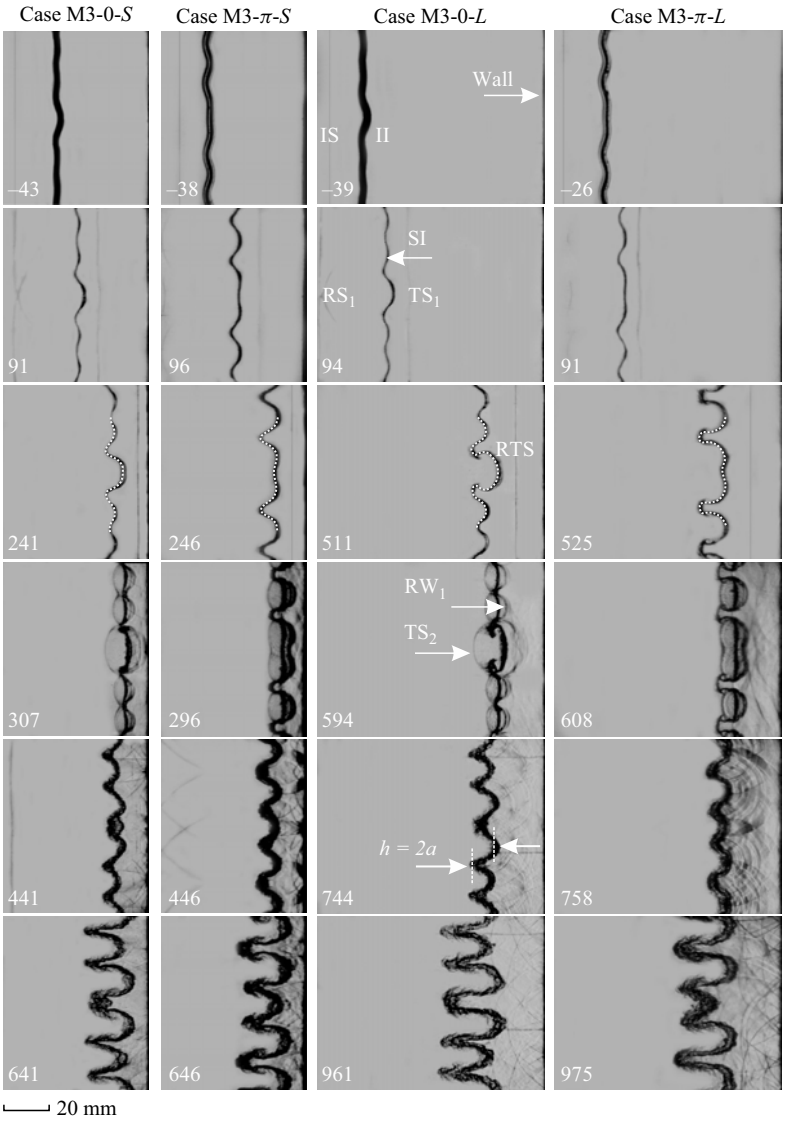


Figure 9. Sequences of schlieren images for various triple-mode cases. The unit of numbers is μs. The symbols are the same as those in figure 3.

$$V_k^M = V_k^{lin} + \frac{1}{2}A_r^+ k_1 \left[\left(1+\sqrt{2}\right) V_k^{lin} a_{2k}^+ + \left(1+\frac{\sqrt{2}}{2}\right) V_{2k}^{lin} a_k^+ \right] + \frac{1}{2}A_r^+ k_1 \left[\left(1+\sqrt{\frac{3}{2}}\right) V_{2k}^{lin} a_{3k}^+ + \left(1+\sqrt{\frac{2}{3}}\right) V_{3k}^{lin} a_{2k}^+ \right] + \frac{1}{2}A_r^+ k_1 \left[\left(1+\sqrt{\frac{3}{4}}\right) V_{3k}^{lin} a_{4k}^+ + \left(1+\sqrt{\frac{3}{4}}\right) V_{4k}^{lin} a_{3k}^+ \right] + \frac{1}{2}A_r^+ k_1 \left[\left(1+\sqrt{\frac{5}{4}}\right) V_{4k}^{lin} a_{5k}^+ + \left(1+\sqrt{\frac{4}{5}}\right) V_{5k}^{lin} a_{4k}^+ \right]$$

https://doi.org/10.1017/jfm.2025.10377 Published online by Cambridge University Press

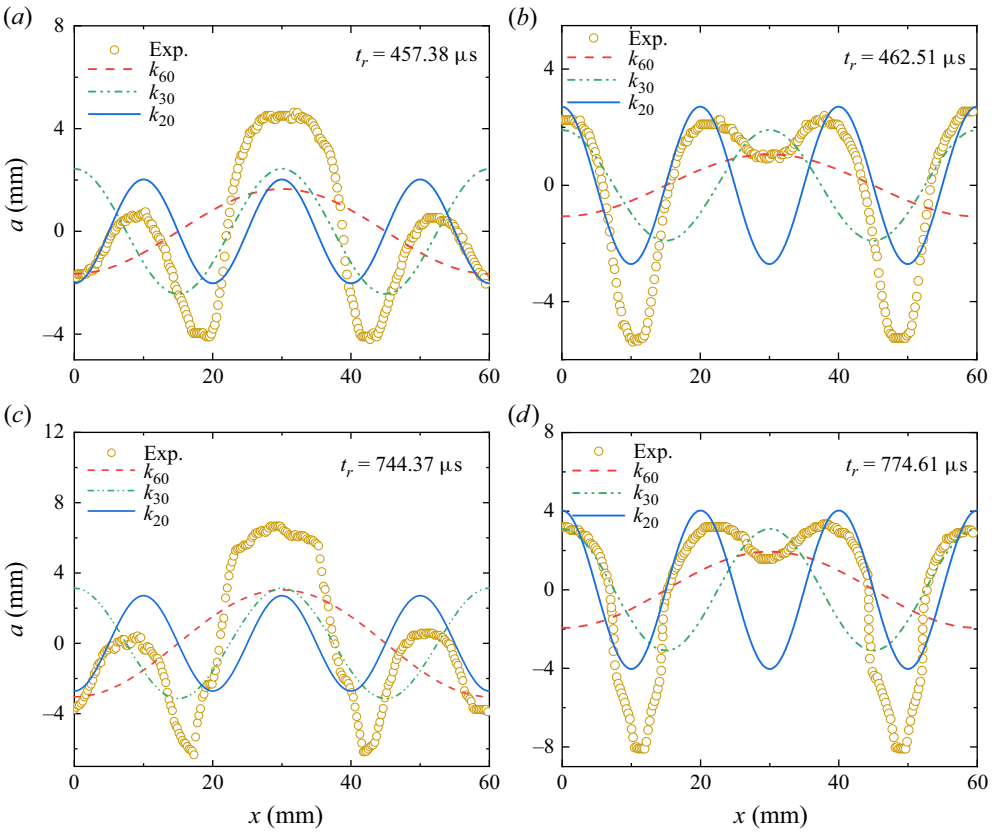


Figure 10. Morphologies of the interface extracted from schlieren images and the basic modes obtained with Fourier analysis at the time of reshock for (*a*) case M3-0-*S*, (*b*) case M3-π-*S*, (*c*) case M3-0-*L* and (*d*) case M3-π-*L*.

$$+\frac{1}{2}A_r^+k_1\left[\left(1+\sqrt{\frac{6}{5}}\right)V_{5k}^{lin}a_{6k}^+ + \left(1+\sqrt{\frac{5}{6}}\right)V_{6k}^{lin}a_{5k}^+\right], \tag{5.1}$$

$$\begin{aligned} V_{2k}^M = V_{2k}^{lin} &- A_r^+k_2V_k^{lin}a_k^+ \\ &+\frac{1}{2}A_r^+k_2\left[\left(1+\sqrt{3}\right)V_k^{lin}a_{3k}^+ + \left(1+\sqrt{\frac{1}{3}}\right)V_{3k}^{lin}a_k^+\right] \\ &+\frac{1}{2}A_r^+k_2\left[\left(1+\sqrt{2}\right)V_{2k}^{lin}a_{4k}^+ + \left(1+\frac{\sqrt{2}}{2}\right)V_{4k}^{lin}a_{2k}^+\right] \\ &+\frac{1}{2}A_r^+k_2\left[\left(1+\sqrt{\frac{5}{3}}\right)V_{3k}^{lin}a_{5k}^+ + \left(1+\sqrt{\frac{3}{5}}\right)V_{5k}^{lin}a_{3k}^+\right] \\ &+\frac{1}{2}A_r^+k_2\left[\left(1+\sqrt{\frac{3}{2}}\right)V_{4k}^{lin}a_{6k}^+ + \left(1+\sqrt{\frac{2}{3}}\right)V_{6k}^{lin}a_{4k}^+\right], \end{aligned} \tag{5.2}$$

https://doi.org/10.1017/jfm.2025.10377 Published online by Cambridge University Press

Case	a_{rk}^{-} (mm)	a_{r2k}^{-} (mm)	a_{r3k}^{-} (mm)	a_{r4k}^{+} (mm)	a_{r5k}^{+} (mm)	a_{r6k}^{+} (mm)	V_{4k}^{lin} ($\mathrm{m\,s^{-1}}$)	V_{5k}^{lin} ($\mathrm{m\,s^{-1}}$)	V_{6k}^{lin} ($\mathrm{m\,s^{-1}}$)	$\mathrm{d}a_1/\mathrm{d}t_k$ ($\mathrm{m\,s^{-1}}$)	$\mathrm{d}a_1/\mathrm{d}t_{2k}$ ($\mathrm{m\,s^{-1}}$)	$\mathrm{d}a_1/\mathrm{d}t_{3k}$ ($\mathrm{m\,s^{-1}}$)
M3-0-*S*	1.65	2.44	2.02	0.43	0.14	0.18	−4.62	1.54	−1.96	4.74	7.68	3.74
M3-π-*S*	1.07	1.91	2.71	0.22	0.71	0.57	−2.3	1.97	−1.54	4.18	3.72	6.1
M3-0-*L*	3.04	3.14	2.71	0.60	0.11	0.03	−10.02	2.10	−1.49	4.78	1.5	0.8
M3-π-*L*	1.94	3.10	4.03	0.57	0.97	0.29	4.23	−0.50	−0.71	3.05	1.93	3.47

Table 5. Main parameters corresponding to the perturbation growth in triple-mode cases. Here, a_r^{-} refers to the interface amplitude at the moment before the reshock, a_r^{+} to the interface amplitude at the moment after the reshock, V^{lin} to the post-reshock growth rate of the interface, $\mathrm{d}a_1/\mathrm{d}t$ to the pre-reshock growth rate of the interface and '+' and '−' denote whether the phase is in phase with the first-order fundamental mode (+) or out of phase with it (−).

$$
\begin{aligned}
V_{3k}^{M} = V_{3k}^{lin} &- \frac{1}{2}A_r^{+}k_3\left[\left(1+\sqrt{2}\right)V_k^{lin}a_{2k}^{+} + \left(1+\frac{\sqrt{2}}{2}\right)V_{2k}^{lin}a_k^{+}\right] \\
&+ \frac{1}{2}A_r^{+}k_3\left(3V_k^{lin}a_{4k}^{+} + \frac{3}{2}V_{4k}^{lin}a_k^{+}\right) \\
&+ \frac{1}{2}A_r^{+}k_3\left[\left(1+\sqrt{\frac{5}{2}}\right)V_{2k}^{lin}a_{5k}^{+} + \left(1+\sqrt{\frac{2}{5}}\right)V_{5k}^{lin}a_{2k}^{+}\right] \\
&+ \frac{1}{2}A_r^{+}k_3\left[\left(1+\sqrt{2}\right)V_{3k}^{lin}a_{6k}^{+} + \left(1+\frac{\sqrt{2}}{2}\right)V_{6k}^{lin}a_{3k}^{+}\right]. \qquad (5.3)
\end{aligned}
$$

Similarly, by employing asymptotic matching as in (4.10), the post-reshock growth rates of the fundamental modes can be calculated. Note that, in the calculation, the amplitudes of the fourth, fifth and sixth harmonics are measured experimentally, as listed in table 5. The temporal variations of the amplitudes of the three fundamental modes after reshock are plotted in figure 11. As shown, the model provides accurate predictions for the growth of all fundamental modes. An exception is the growth of the $3k$ mode in case M3-π-*L* after 150 μs. This deviation is ascribed to stronger nonlinearity in this case, as evidenced by earlier saturation, which exceeds the application range of the present model. Specifically, the pre-reshock amplitude-to-wavelength ratio of the $3k$ mode for case M3-π-*L* is 1.27. This higher ratio leads to a rapid approach to nonlinear saturation due to the high initial growth rate, which contradicts the current model. Equations (4.8) and (4.9) do incorporate a second-order approximation of mode-coupling effects, based on the assumption that these interactions occur primarily during the reshock event. This approximation captures the early post-reshock evolution reasonably well, particularly when the interface amplitude is still small and the nonlinear interactions are relatively weak. However, as the interface evolution enters a strongly nonlinear regime, higher-order mode interactions become increasingly significant and are no longer adequately represented by the simplified coupling terms derived under impulsive assumptions. In particular, these equations, which are derived from Haan's second-order weakly nonlinear model, fail to account for the sustained mode interactions and vortex-merging dynamics that persists long after the passage of the shock. Therefore, while (4.8) and (4.9) account for initial mode coupling, their assumptions break down at later times, explaining the model–data discrepancy in the strongly nonlinear phase.

https://doi.org/10.1017/jfm.2025.10377 Published online by Cambridge University Press

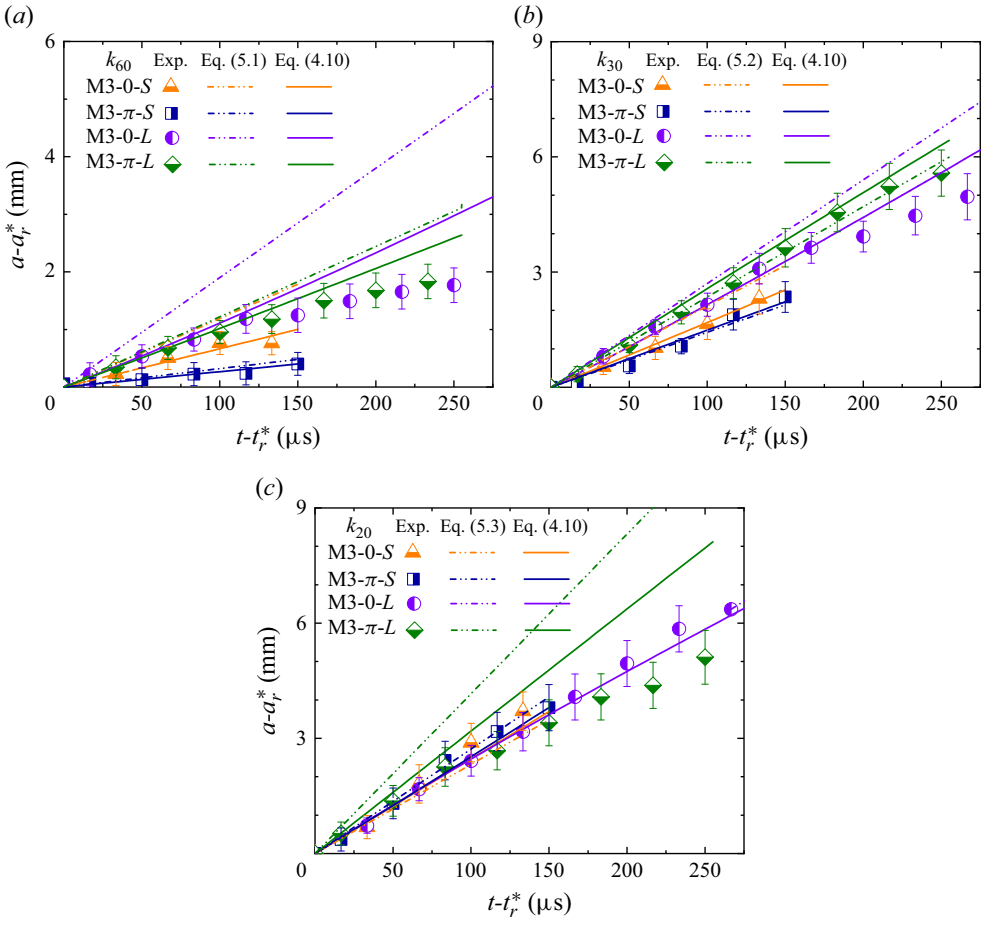


Figure 11. The amplitude growths of modes (*a*) k , (*b*) $2k$ and (*c*) $3k$ for triple-mode cases following reshock.

6. Correlation between the post-reshock growth rate and the pre-reshock interface shape

The above results demonstrate that mode-coupling effects play a crucial role in the evolution of reshocked RMI at both dual- and triple-mode interfaces. Additionally, the results for single-mode RMI reveal that as harmonic amplitudes become relatively large, existing models that ignore harmonic generation become less accurate. These findings suggest that neglecting mode-coupling effects could be a crucial factor for the failure of model prediction. To validate this hypothesis, we use Fourier analysis to examine the mode compositions of all interfaces considered in this study at the time of reshock. Three single-mode cases with relatively strong nonlinearity are first examined, and their amplitude growths are compared with model predictions. As depicted in figure 12(*a*), the new modal model, which incorporates mode-coupling effects, provides significantly improved predictions compared with the original model. Considering the predicted growth rate is time-dependent, an average growth rate, $\bar{V}^H$, is calculated for each case to facilitate comparison, as detailed in table 6. The comparison between the linear mode and modal mode predictions demonstrates that as higher harmonics emerge, mode-coupling effects become significant and must be accounted for. The time at which the reflected rarefaction wave interacts with the interface under short, long and extended reflection distances

https://doi.org/10.1017/jfm.2025.10377 Published online by Cambridge University Press

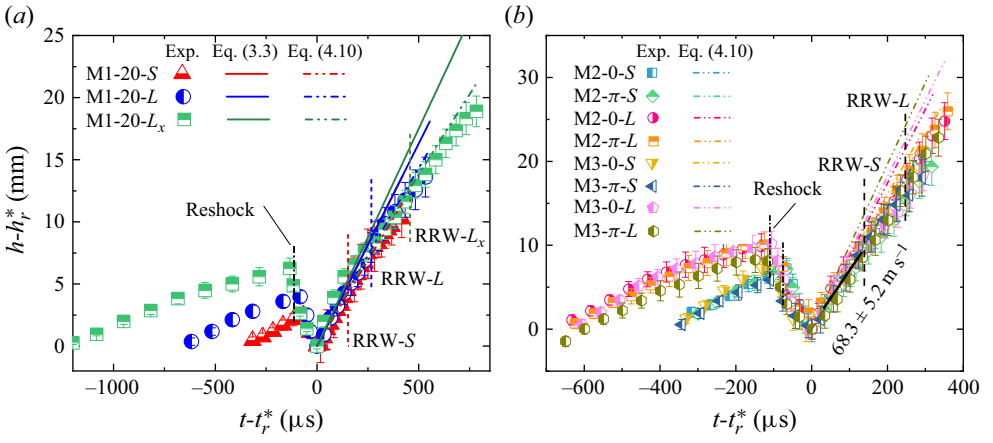


Figure 12. The growth of the mixing width for (*a*) single-mode, (*b*) dual-mode and triple-mode interfaces. The solid lines denote the prediction of (3.3), the dash-dot-dotted lines denote the prediction of (4.10), and the dashed lines indicate the time at which the reflected rarefaction wave (RRW_1) interacts with the interface. Note that the time at which the reflected rarefaction wave interacts with the interface under short, long and extended reflection distances, are respectively labelled as RRW-S, RRW-L and RRW-L_x.

Case	ka_{kr}	$2ka_{2kr}$	da_2/dt (m s^{-1})	$\bar{V}^{lin}$ (m s^{-1})	$\bar{V}^{H}$ (m s^{-1})
M1-60-S	0.20	−0.01	7.2	7.2	7.2
M1-40-S	0.38	−0.12	17.1	17.3	17.3
M1-30-S	0.58	−0.25	19.3	19.7	19.3
M1-20-S	1.07	−0.53	28.2	28.6	27.3
M1-60-L	0.34	−0.07	16.0	16.3	16.2
M1-40-L	0.63	−0.21	23.9	24.7	24.3
M1-30-L	1.02	−0.37	28.1	28.9	27.8
M1-20-L	1.38	−0.89	28.7	35.6	28.0
M1-30-L^+	1.32	−1.09	22.6	36.0	25.8

Table 6. Detailed parameters corresponding to the initial conditions for single-mode cases. Here, ka_{kr} refers to the product of wavenumber and amplitude at reshock for low-order interface, $2ka_{2kr}$ to the product of wavenumber and amplitude at reshock for second-order interface, '−' indicates the opposite phase of the low-order interface, da_2/dt refers to the post-reshock growth rate of the interface, V^{lin} to growth rate after reshock calculated with (3.3) and $\bar{V}^{H}$ to the average growth rate after reshock calculated with (4.10).

marked in figure 12(*a*) indicates that nonlinear growth of the interface is already evident in all cases before the arrival of RRW_1. This exludes the possibility that the post-reshock growth rate is influenced by the subsequent wave interactions. Similar interface growth behaviour following reshock has been observed across diverse shock-tube experiments and simulations (Vetter & Sturtevant 1995; Bin *et al.* 2021; Guo *et al.* 2022*b*; Wang *et al.* 2022; Cao *et al.* 2024; Xie *et al.* 2025). This behaviour is likely associated with the onset of turbulent mixing (Thornber *et al.* 2017; Kokkinakis, Drikakis & Youngs 2020; Soulard & Griffond 2022; Zhou, Ding & Cheng 2024).

Temporal variations of the interface amplitude for the dual- and triple-mode cases are plotted in figure 12(*b*). It is observed that the dual- and triple-mode interfaces with different mode compositions and phase combinations present nearly identical growth rates after reshock. This observation is consistent with the previous findings of Leinov *et al.*

https://doi.org/10.1017/jfm.2025.10377 Published online by Cambridge University Press

Case	M1-60-S	M1-40-S	M1-30-S	M1-20-S	M1-60-L	M1-40-L	M1-30-L	M1-20-L	M1-30-L^+
$\bar{k}a_{r0}$	0.20	0.38	0.58	1.07	0.34	0.63	1.02	1.39	1.38
β	0.25	0.48	0.55	0.70	0.43	0.55	0.69	0.64	0.45
β^H	0.25	0.48	0.55	0.69	0.43	0.56	0.69	0.62	0.51
Case	M2-0-S	M2-π-S	M2-0-L	M2-π-L	M3-0-S	M3-π-S	M3-0-L	M3-π-L	
$\bar{k}a_{r0}$	0.97	1.11	1.31	1.68	1.11	1.04	1.41	1.59	
β	0.86	0.85	0.93	0.88	0.90	0.88	0.93	0.90	
β^H	0.90	0.88	1.07	0.97	1.04	0.93	1.12	1.11	

Table 7. Here, β and β^H refer to the factors calculated using (6.1) and (6.2), respectively. β^H is a linear fit with time.

(2009) regarding reshocked RMI at initial random multi-mode interfaces. However, for the single-mode case, the post-reshock growth rate is closely related to the initial interface morphology, consistent with recent findings (Guo *et al.* 2022*a*; Zhang *et al.* 2023*b*). This raises an interesting yet crucial question: Under what conditions does the post-reshock growth rate depend on the pre-reshock interface morphology?

Charakhch'An (2000) found that the post-reshock growth rate shows a weak dependence on the pre-reshock amplitude and wavenumber, but is closely related to the pre-reshock growth rate. Based on this finding, an empirical model was proposed

$$\frac{\mathrm{d}h_2}{\mathrm{d}t} = \beta \Delta V_2 A_r^+ - \frac{\mathrm{d}h_1}{\mathrm{d}t}, \tag{6.1}$$

where h_2 is the overall width of the mixing zone (i.e. the distance between the spike and bubble tips) and $\mathrm{d}h_1/\mathrm{d}t$ is the growth rate of the mixing width just before reshock. The value of $\beta = 1.25$, which represents the average of β values ranging from 0.53 to 1.5 across various cases, was suggested.

The post-reshock growth rate for the basic modes and harmonics can be predicted by the modal model: $V_r(t) = V_k^H(t)\cos(kx + \phi_k) + \sum_{n>1} V_{nk}^H(t)\cos(nkx + \phi_{nk})$, where $V^H(t)$ is the growth rate after reshock calculated using (4.10). Based on (6.1), β can be expressed as

$$\beta^H(t) = \frac{(|V_r^{max}(t)| + |V_r^{min}(t)|) + (|V_1^{max}| + |V_1^{min}|)}{\Delta V_2 A_r^+}, \tag{6.2}$$

with $V_1 = \mathrm{d}a_1/\mathrm{d}t_k \cos(kx + \phi_k) + \sum_{n>1} \mathrm{d}a_1/\mathrm{d}t_{nk} \cos(nkx + \phi_{nk})$, $(n = 1, 2, 3)$ representing the interface growth rate prior to reshock. As indicated in table 7, (6.2) provides reasonable predictions for the value of β across all single-, dual- and triple-mode cases examined in this study.

To facilitate comparison among the single-, dual- and triple-mode cases, the experimental data are normalised using the method of Gowardhan, Ristorcelli & Grinstein (2011). For a multi-mode interface, the characteristic wavenumber is calculated by the weighted average wavenumber

$$\bar{k} = \sqrt{\frac{\sum_{i=1}^{n} a_{ik}^2 k_{ik}^2}{\sum_{i=1}^{n} a_{ik}^2}}. \tag{6.3}$$

The relationship between β and $\bar{k}a_{r0}$ for all cases is shown in figure 13. As we can see, for the single-mode case, β is closely related to $\bar{k}a_{r0}$, whereas for the multi-mode case, where

https://doi.org/10.1017/jfm.2025.10377 Published online by Cambridge University Press

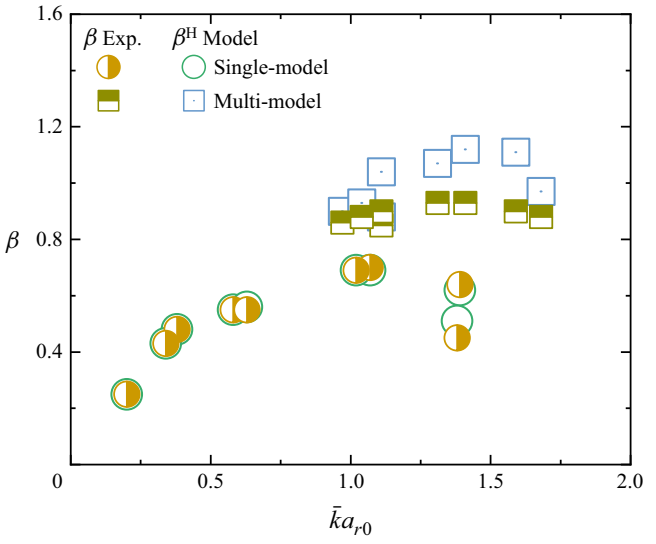


Figure 13. The variation of β with $\bar{k}a_{r0}$.

nonlinearity becomes more pronounced, β shows only a weak dependence on $\bar{k}a_{r0}$. The present finding provides a sound explanation for the varying degrees of dependence of β on $\bar{k}a_{r0}$ in single- and multi-mode configurations under reshock conditions.

7. Conclusions

This work presents a comprehensive experimental and theoretical investigation of reshocked RMI. Through a soap-film technique, we achieve unprecedented control over initial interface shape, successfully generating well-defined single-, dual- and triple-mode air/SF_6 interfaces. The reflected shock is created by an acrylic block inserted into the test section. This experimental design facilitates precise control over both interface morphology and reshock timing, enabling a systematic exploration of the relationship between post-reshock instability growth and initial perturbation spectra.

The results reveal distinct dependencies of the post-reshock growth rate on the pre-reshock interface morphology across different configurations. For single-mode interfaces, the post-reshock growth rate strongly correlates with pre-reshock conditions. In contrast, for multi-mode interfaces, this dependence weakens significantly. This is attributed to enhanced mode-coupling effects in multi-mode configurations, a crucial physical mechanism that has been inadequately addressed in existing theoretical models. To bridge this gap, we develop an empirical modal model that matches the initial linear growth and the asymptotic growth rate accounting for mode-coupling effects. The model demonstrates excellent predictive capability across all experimental configurations, from single-mode to more complex triple-mode cases. Furthermore, a unified formula relating the empirical coefficient β in Charakhch'An's model (Charakhch'An 2000) to initial perturbation characteristics is derived. This provides, for the first time, a coherent theoretical framework that explains the varying dependence of post-reshock growth rates on pre-reshock morphology observed across different experimental configurations. The comprehensive understanding gained through this work has significant implications for applications involving reshocked RMI, particularly in ICF and supersonic combustion systems. Our future work will focus on extending this framework to more complex

https://doi.org/10.1017/jfm.2025.10377 Published online by Cambridge University Press

interface configurations and investigating the transition to turbulent mixing under reshock conditions.

Funding. This work was supported by the National Natural Science Foundation of China (nos. 12388101, 12402259), the National Key Research and Development Program of China (2022YFF0504500), the Strategic Priority Research Program of Chinese Academy of Science (XDB1100120, XDB0500301) and the Laoshan Laboratory (LSKJ202300305).

Declaration of interests. The authors report no conflict of interest.

References

ALON, U., HECHT, J., OFER, D. & SHVARTS, D. 1995 Power laws and similarity of Rayleigh–Taylor and Richtmyer–Meshkov mixing fronts. *Phys. Rev. Lett.* **74** (4), 534–537.

AURE, R. & JACOBS, J.W. 2008 Particle image velocimetry study of the shock-induced single mode Richtmyer–Meskov instability. *Shock Waves* **18** (3), 161–167.

BALAKUMAR, B.J., ORLICZ, G.C., RISTORCELLI, J.R., BALASUBRAMANIAN, S., PRESTRIDGE, K.P. & TOMKINS, C.D. 2012 Turbulent mixing in a Richtmyer–Meshkov fluid layer after reshock: velocity and density statistics. *J. Fluid Mech.* **696**, 67–93.

BALAKUMAR, B.J., ORLICZ, G.C., TOMKINS, C.D. & PRESTRIDGE, K.P. 2008*a* Dependence of growth patterns and mixing width on initial conditions in Richtmyer–Meshkov unstable fluid layers. *Phys. Scr.* **T132**, 014013.

BALAKUMAR, B.J., ORLICZ, G.C., TOMKINS, C.D. & PRESTRIDGE, K.P. 2008*b* Simultaneous particle-image velocimetry–planar laser-induced fluorescence measurements of Richtmyer–Meshkov instability growth in a gas curtain with and without reshock. *Phys. Fluids* **20** (12), 124103.

BALASUBRAMANIAN, S., ORLICZ, G.C., PRESTRIDGE, K.P. & BALAKUMAR, B.J. 2012 Experimental study of initial condition dependence on Richtmyer–Meshkov instability in the presence of reshock. *Phys. Fluids* **24** (3), 034103.

BIN, Y., XIAO, M., SHI, Y., ZHANG, Y. & CHEN, S. 2021 A new idea to predict reshocked Richtmyer–Meshkov mixing: constrained large-eddy simulation. *J. Fluid Mech.* **918**, R1.

BROUILLETTE, M. 2002 The Richtmyer–Meshkov instability. *Annu. Rev. Fluid Mech.* **34** (1), 445–468.

BUTTLER, W.T. 2012 Unstable Richtmyer–Meshkov growth of solid and liquid metals in vacuum. *J. Fluid Mech.* **703**, 60–84.

CAO, Q., CHEN, C., WANG, H., ZHAI, Z. & LUO, X. 2024 Interface evolution induced by two successive shocks under diverse reshock conditions. *J. Fluid Mech.* **999**, A31.

CHARAKHCH'AN, A.A. 2000 Richtmyer–Meshkov instability of an interface between two media due to passage of two successive shocks. *J. Appl. Mech. Tech. Phys.* **41** (1), 23–31.

CHEN, C., WANG, H., ZHAI, Z. & LUO, X. 2024 Mode coupling between two different interfaces of a gas layer subject to a shock. *J. Fluid Mech.* **984**, A38.

CLOUTMAN, L.D. & WEHNER, M.F. 1992 Numerical simulation of Richtmyer–Meshkov instabilities. *Phys. Fluids A* **4** (8), 1821–1830.

COHEN, R.D. 1991 Shattering of a liquid drop due to impact. *Proc. R. Soc. Lond. A: Math. Phys. Sci.* **435** (1895), 483–503.

DIMONTE, G. & RAMAPRABHU, P. 2010 Simulations and model of the nonlinear Richtmyer–Meshkov instability. *Phys. Fluids* **22** (1), 014104.

DING, J., SI, T., CHEN, M., ZHAI, Z., LU, X. & LUO, X. 2017*a* On the interaction of a planar shock with a three-dimensional light gas cylinder. *J.Fluid Mech.* **828**, 289–317.

DING, J., SI, T., YANG, J., LU, X., ZHAI, Z. & LUO, X. 2017*b* Measurement of a Richtmyer–Meshkov instability at an air-SF_6 interface in a semiannular shock tube. *Phys. Rev. Lett.* **119** (1), 014501.

FERGUSON, K. & JACOBS, J.W. 2024 The influence of the shock-to-reshock time on the Richtmyer–Meshkov instability in reshock. *J. Fluid Mech.* **999**, A68.

GIBSON, C. 1968 Fine structure of scalar fields mixed by turbulence. II. Spectral theory. *Phys. Fluids* **11** (11), 2316–2327.

GOWARDHAN, A.A., RISTORCELLI, J.R. & GRINSTEIN, F.F. 2011 The bipolar behavior of the Richtmyer–Meshkov instability. *Phys. Fluids* **23** (7), 071701.

GUO, X., CONG, Z., SI, T. & LUO, X. 2022*a* Shock-tube studies of single- and quasi-single-mode perturbation growth in Richtmyer–Meshkov flows with reshock. *J. Fluid Mech.* **941**, A65.

GUO, X., SI, T., ZHAI, Z. & LUO, X. 2022*b* Large-amplitude effects on interface perturbation growth in Richtmyer–Meshkov flows with reshock. *Phys. Fluids* **34** (8), 082118.

https://doi.org/10.1017/jfm.2025.10377 Published online by Cambridge University Press

HAAN, S.W. 1991 Weakly nonlinear hydrodynamic instabilities in inertial fusion. *Phys. Fluids B* **3** (8), 2349–2355.

JACOBS, J.W., JENKINS, D.G., KLEIN, D.L. & BENJAMIN, R.F. 1995 Nonlinear growth of the shock-accelerated instability of a thin fluid layer. *J. Fluid Mech.* **295**, 23–42.

JACOBS, J.W. & KRIVETS, V.V. 2005 Experiments on the late-time development of single-mode Richtmyer–Meshkov instability. *Phys. Fluids* **17** (3), 034105.

JACOBS, J.W., KRIVETS, V.V. & TSIKLASHVILI, V. 2013 Experiments on the Richtmyer–Meshkov instability with an imposed, random initial perturbation. *Shock Waves* **23** (4), 407–413.

JACOBS, J.W. & SHEELEY, J.M. 1996 Experimental study of incompressible Richtmyer–Meshkov instability. *Phys. Fluids* **8** (2), 405–415.

KOKKINAKIS, I.W., DRIKAKIS, D. & YOUNGS, D.L. 2020 Vortex morphology in Richtmyer–Meshkov-induced turbulent mixing. *Physica D* **407**, 132459.

KUNDU, P.K., COHEN, I. & DOWLING, D. 2012 Kinematics. In *Fluid Mechanics*. 5th edn, pp. 85–88. Elsevier Inc.

KURANZ, C.C. 2018 How high energy fluxes may affect Rayleigh–Taylor instability growth in young supernova remnants. *Nat. Commun.* **9** (1), 1564.

LATINI, M., SCHILLING, O. & DON, W.S. 2007 High-resolution simulations and modeling of reshocked single-mode Richtmyer–Meshkov instability: comparison to experimental data and to amplitude growth model predictions. *Phys. Fluids* **19** (2), 024104.

LEINOV, E., MALAMUD, G., ELBAZ, Y., LEVIN, L.A., BEN-DOR, G., SHVARTS, D. & SADOT, O. 2009 Experimental and numerical investigation of the Richtmyer–Meshkov instability under re-shock conditions. *J. Fluid Mech.* **626**, 449–475.

LI, J., DING, J., LUO, X. & ZOU, L. 2022*a* Instability of a heavy gas layer induced by a cylindrical convergent shock. *Phys. Fluids* **34** (4), 042123.

LI, J., YAN, R., ZHAO, B., ZHENG, J., ZHANG, H. & LU, X. 2022*b* Mitigation of the ablative Rayleigh–Taylor instability by nonlocal electron heat transport. *Matt. Radiat. Extremes* **7** (5), 8.

LI, Y., SAMTANEY, R. & WHEATLEY, V. 2018 The Richtmyer–Meshkov instability of a double-layer interface in convergent geometry with magnetohydrodynamics. *Matt. Radiat. Extremes* **3** (4), 12.

LINDL, J., LANDEN, O., EDWARDS, J., MOSES, E. & TEAM, N. 2014 Review of the National Ignition Campaign 2009–2012. *Phys. Plasmas* **21** (2), 020501.

LIU, L., LIANG, Y., DING, J., LIU, N. & LUO, X. 2018 An elaborate experiment on the single-mode Richtmyer–Meshkov instability. *J. Fluid Mech.* **853**, R2.

LUO, X., LIU, L., LIANG, Y., DING, J. & WEN, C. 2020 Richtmyer–Meshkov instability on a dual-mode interface. *J. Fluid Mech.* **905**, A5.

MANSOOR, M.M., DALTON, S.M., MARTINEZ, A.A., DESJARDINS, T., CHARONKO, J.J. & PRESTRIDGE, K.P. 2020 The effect of initial conditions on mixing transition of the Richtmyer–Meshkov instability. *J. Fluid Mech.* **904**, A3.

MESHKOV, E.E. 1969 Instability of the interface of two gases accelerated by a shock wave. *Fluid Dyn.* **4** (5), 101–104.

MIKAELIAN, K.O. 1985 Richtmyer–Meshkov instabilities in stratified fluids. *Phys. Rev. A* **31** (1), 410–419.

MIKAELIAN, K.O. 1989 Turbulent mixing generated by Rayleigh–Taylor and Richtmyer–Meshkov instabilities. *Physica D* **36**, 343–357.

MIKAELIAN, K.O. 2005 Rayleigh–Taylor and Richtmyer–Meshkov instabilities and mixing in stratified cylindrical shells. *Phys. Fluids* **17** (9), 094105.

MOHAGHAR, M., CARTER, J., MUSCI, B., REILLY, D., MCFARLAND, J. & RANJAN, D. 2017 Evaluation of turbulent mixing transition in a shock-driven variable-density flow. *J. Fluid Mech.* **831**, 779–825.

MOHAGHAR, M., CARTER, J., PATHIKONDA, G. & RANJAN, D. 2019 The transition to turbulence in shock-driven mixing: effects of Mach number and initial conditions. *J. Fluid Mech.* **871**, 595–635.

MORGAN, R.V., AURE, R., STOCKERO, J.D., GREENOUGH, J.A., CABOT, W., LIKHACHEV, O.A., JACOBS, J.W. 2012 On the late-time growth of the two-dimensional Richtmyer–Meshkov instability in shock tube experiments. *J. Fluid Mech.* **712**, 354–383.

MURAKAMI, M. & NISHI, D. 2017 Optimization of laser illumination configuration for directly driven inertial confinement fusion. *Matt. Radiat. Extremes* **2** (2), 14–68.

NOBLE, C.D., AMES, A.M., MCCONNELL, R., OAKLEY, J., ROTHAMER, D.A. & BONAZZA, R. 2023 Simultaneous measurements of kinetic and scalar energy spectrum time evolution in the Richtmyer–Meshkov instability upon reshock. *J. Fluid Mech.* **975**, A39.

OFER, D., ALON, U., SHVARTS, D., MCCRORY, R.L. & VERDON, C.P. 1996 Modal model for the nonlinear multimode Rayleigh–Taylor instability. *Phys. Plasmas* **3** (8), 3073–3090.

PROBYN, M.G., WILLIAMS, R.J.R., THORNBER, B., DRIKAKIS, D. & YOUNGS, D.L. 2021 2D single-mode Richtmyer–Meshkov instability. *Physica D* **418**, 132827.

https://doi.org/10.1017/jfm.2025.10377 Published online by Cambridge University Press

RANJAN, D. 2008 Shock-bubble interactions: features of divergent shock-refraction geometry observed in experiments and simulations. *Phys. Fluids* **20** (3), 036101.

RANJAN, D., OAKLEY, J. & BONAZZA, R. 2011 Shock-bubble interactions. *Annu. Rev. Fluid Mech.* **43** (1), 117–140.

RICHTMYER, R.D. 1960 Taylor instability in shock acceleration of compressible fluids. *Commun. Pure Appl. Maths* **13** (2), 297–319.

SADOT, O., EREZ, L., ALON, U., ORON, D., LEVIN, L.A., EREZ, G., BEN-DOR, G. & SHVARTS, D. 1998 Study of nonlinear evolution of single-mode and two-bubble interaction under Richtmyer–Meshkov instability. *Phys. Rev. Lett.* **80** (8), 1654–1657.

SAMTANEY, R., RAY, J. & ZABUSKY, N.J. 1998 Baroclinic circulation generation on shock accelerated slow/fast gas interfaces. *Phys. Fluids* **10** (5), 1217–1230.

SAMTANEY, R. & ZABUSKY, N.J. 1994 Circulation deposition on shock-accelerated planar and curved density-stratified interfaces: models and scaling laws. *J. Fluid Mech.* **269**, 45–78.

SAMULSKI, C., SRINIVASAN, B., MANUEL, J.E., MASTI, R., SAUPPE, J.P. & KLINE, J. 2022 Deceleration-stage Rayleigh–Taylor growth in a background magnetic field studied in cylindrical and Cartesian geometries. *Matt. Radiat. Extremes* **7** (2), 12.

SEWELL, E.G., FERGUSON, K.J., KRIVETS, V.V. & JACOBS, J.W. 2021 Time-resolved particle image velocimetry measurements of the turbulent Richtmyer–Meshkov instability. *J. Fluid Mech.* **917**, A41.

SOHN, S. 2011 Inviscid and viscous vortex models for Richtmyer–Meshkov instability. *Fluid Dyn. Res.* **43** (6), 1–17.

SOHN, S.I. 2003 Simple potential-flow model of Rayleigh–Taylor and Richtmyer–Meshkov instabilities for all density ratios. *Phys. Rev. E* **67** (2), 026301.

SOULARD, O. & GRIFFOND, J. 2022 Permanence of large eddies in Richtmyer–Meshkov turbulence for weak shocks and high Atwood numbers. *Phys. Rev. Fluids* **7** (1), 014605.

THORNBER, B. 2017 Late-time growth rate, mixing, and anisotropy in the multimode narrowband Richtmyer–Meshkov instability: the θ-group collaboration. *Phys. Fluids* **29** (10), 105107.

UKAI, S., BALAKRISHNAN, K. & MENON, S. 2011 Growth rate predictions of single- and multi-mode Richtmyer–Meshkov instability with reshock. *Shock Waves* **21** (6), 533–546.

URZAY, J. 2018 Supersonic combustion in air-breathing propulsion systems for hypersonic flight. *Annu. Rev. Fluid Mech.* **50** (1), 593–627.

VANDENBOOMGAERDE, M., CHERFILS, C., GALMICHE, D., GAUTHIER, S. & RAVIART, P.A. 2003 Efficient perturbation methods for Richtmyer–Meshkov and Rayleigh–Taylor instabilities: weakly nonlinear stage and beyond. *Laser Part. Beams* **21** (3), 321–325.

VANDENBOOMGAERDE, M., GAUTHIER, S. & MÜGLER, C. 2002 Nonlinear regime of a multimode Richtmyer–Meshkov instability: a simplified perturbation theory. *Phys. Fluids* **14** (3), 1111–1122.

VANDENBOOMGAERDE, M., MÜGLER, C. & GAUTHIER, S. 1998 Impulsive model for the Richtmyer–Meshkov instability. *Phys. Rev. E* **58** (2), 1874–1882.

VETTER, M. & STURTEVANT, B. 1995 Experiments on the Richtmyer–Meshkov instability of an air/SF_6 interface. *Shock Waves* **4**, 247–252.

WANG, H., DING, J., SI, T. & LUO, X. 2022 Richtmyer–Meshkov instability of a single-mode interface with reshock. *Acta Aerodyn. Sin.* **40** (1), 33–40.

WANG, M., SI, T. & LUO, X. 2013 Generation of polygonal gas interfaces by soap film for Richtmyer–Meshkov instability study. *Exp. Fluids* **54** (1), 1427.

WEBER, C., HAEHN, N., OAKLEY, J., ANDERSON, M. & BONAZZA, R. 2012 Richtmyer–Meshkov instability on a low Atwood number interface after reshock. *Shock Waves* **22** (4), 317–325.

XIE, H., QI, H., XIAO, M., ZHANG, Y. & ZHAO, Y. 2025 An intermittency based Reynolds-averaged transition model for mixing flows induced by interfacial instabilities. *J. Fluid Mech.* **1002**, A31.

YOUNGS, D.L. 1994 Numerical simulation of mixing by Rayleigh–Taylor and Richtmyer–Meshkov instabilities. *Laser Part. Beams* **12** (4), 725–750.

YOUNGS, D.L. & WILLIAMS, R.J. 2008 Turbulent mixing in spherical implosions. *Intl J. Numer. Meth. Fluids* **56** (8), 1597–1603.

ZABUSKY, N.J. 1999 Vortex paradigm for accelerated inhomogeneous flows: visiometrics for the Rayleigh–Taylor and Richtmyer–Meshkov environments. *Annu. Rev. Fluid Mech.* **31** (1), 495–536.

ZHANG, D., DING, J., SI, T. & LUO, X. 2023*a* Divergent Richtmyer–Meshkov instability on a heavy gas layer. *J. Fluid Mech.* **959**, A37.

ZHANG, Q., DENG, S. & GUO, W. 2018 Quantitative theory for the growth rate and amplitude of the compressible Richtmyer–Meshkov instability at all density ratios. *Phys. Rev. Lett.* **121** (17), 174502.

ZHANG, Q. & GUO, W. 2016 Universality of finger growth in two-dimensional Rayleigh–Taylor and Richtmyer–Meshkov instabilities with all density ratios. *J. Fluid Mech.* **786**, 47–61.

https://doi.org/10.1017/jfm.2025.10377 Published online by Cambridge University Press

ZHANG, Q. & SOHN, S.I. 1997 Nonlinear theory of unstable fluid mixing driven by shock wave. *Phys. Fluids* **9** (4), 1106–1124.

ZHANG, Y., ZHAO, Y., DING, J. & LUO, X. 2023*b* Richtmyer–Meshkov instability with a rippled reshock. *J. Fluid Mech.* **968**, A3.

ZHAO, Y., DING, J., HE, D., ZHOU, Z. & LUO, X. 2025 Convergent Richtmyer–Meshkov turbulence by time-resolved planar laser-induced fluorescence measurement. *J. Fluid Mech.* **1007**, A30.

ZHOU, Y. 2017*a* Rayleigh–Taylor and Richtmyer–Meshkov instability induced flow, turbulence, and mixing. I. *Phys. Rep.* **720-722**, 1–136.

ZHOU, Y. 2017*b* Rayleigh–Taylor and Richtmyer–Meshkov instability induced flow, turbulence, and mixing. II. *Phys. Rep.* **723-725**, 1–160.

ZHOU, Z., DING, J. & CHENG, W. 2024 Mixing and inter-scale energy transfer in Richtmyer–Meshkov turbulence. *J. Fluid Mech.* **984**, A56.

https://doi.org/10.1017/jfm.2025.10377 Published online by Cambridge University Press